



HAL
open science

Dictyostelium lacking the single atlastin homolog Sey1 shows aberrant ER architecture, proteolytic processes and expansion of the Legionella -containing vacuole

Dario Hüsler, Bernhard Steiner, Amanda Welin, Bianca Striednig, A. Leoni Leoni Swart, Virginie Molle, Hubert Hilbi, François Letourneur

► **To cite this version:**

Dario Hüsler, Bernhard Steiner, Amanda Welin, Bianca Striednig, A. Leoni Leoni Swart, et al.. Dictyostelium lacking the single atlastin homolog Sey1 shows aberrant ER architecture, proteolytic processes and expansion of the Legionella -containing vacuole. Cellular Microbiology, 2021, 23 (5), 10.1111/cmi.13318 . hal-03364992

HAL Id: hal-03364992

<https://hal.science/hal-03364992>

Submitted on 5 Oct 2021

HAL is a multi-disciplinary open access archive for the deposit and dissemination of scientific research documents, whether they are published or not. The documents may come from teaching and research institutions in France or abroad, or from public or private research centers.

L'archive ouverte pluridisciplinaire **HAL**, est destinée au dépôt et à la diffusion de documents scientifiques de niveau recherche, publiés ou non, émanant des établissements d'enseignement et de recherche français ou étrangers, des laboratoires publics ou privés.

1
2
3 1 ***Dictyostelium* lacking the single atlastin homolog Sey1 shows aberrant ER architecture,**
4
5 2 **proteolytic processes, and expansion of the *Legionella*-containing vacuole**
6
7
8 3

9
10 4 **Dario Hüsler¹, Bernhard Steiner^{1#}, Amanda Welin², Bianca Striednig¹, A. Leoni Swart¹,**
11
12 5 **Virginie Molle³, Hubert Hilbi^{1*}, François Letourneur^{3*}**
13
14 6

15
16
17 7 ¹ Institute of Medical Microbiology, University of Zurich, Gloriastrasse 30, 8006 Zürich,
18
19 8 Switzerland

20
21 9 ² Division of Inflammation and Infection, Department of Biomedical and Clinical Sciences,
22
23 10 Linköping University, 58185 Linköping, Sweden

24
25
26 11 ³ Laboratory of Pathogen Host Interactions, Université de Montpellier, CNRS, INSERM,
27
28 12 Place Eugène Bataillon, Montpellier, 34095 cedex 5, France

29
30 13 Present address: [#]Institute for Molecular Bioscience, University of Queensland, Brisbane,
31
32 14 Queensland 4072, Australia
33
34
35 15

36
37 16 **Running title:** *Dictyostelium* atlastin controls ER architecture and *Legionella* replication

38
39 17 **Key words:** Amoeba, atlastin, *Dictyostelium discoideum*, endocytic pathway, large GTPase,
40
41 18 host-pathogen interaction, *Legionella pneumophila*, Legionnaires' disease, pathogen vacuole,
42
43 19 unfolded protein response.
44
45

46
47 20 **Abbreviations:** Atlastin, ATL; Icm/Dot, intracellular multiplication/defective organelle
48
49 21 trafficking; transmission electron microscopy, TEM; tunicamycin, TN; T4SS, type IV
50
51 22 secretion system; unfolded protein response, UPR.
52
53
54 23

55
56 24 *Correspondence: hilbi@imm.uzh.ch; francois.letourneur@umontpellier.fr
57

58 25 Tel.: +41 (0)44 634 2650; +33 (0)46 714 4731
59
60

26 **ABSTRACT**

27 *Dictyostelium discoideum* Sey1 is the single ortholog of mammalian atlastin 1-3 (ATL1-3),
28 which are large homodimeric GTPases mediating homotypic fusion of endoplasmic reticulum
29 (ER) tubules. In this study, we generated a *D. discoideum* mutant strain lacking the *sey1* gene
30 and found that amoebae deleted for *sey1* are enlarged, but grow and develop similarly to the
31 parental strain. The Δ *sey1* mutant amoebae showed an altered ER architecture, and the tubular
32 ER network was partially disrupted without any major consequences for other organelles or
33 the architecture of the secretory and endocytic pathways. Macropinocytic and phagocytic
34 functions were preserved; however, the mutant amoebae exhibited cumulative defects in
35 lysosomal enzymes exocytosis, intracellular proteolysis, and cell motility, resulting in
36 impaired growth on bacterial lawns. Moreover, Δ *sey1* mutant cells showed a constitutive
37 activation of the unfolded protein response pathway (UPR), but they still readily adapted to
38 moderate levels of ER stress, while unable to cope with prolonged stress. In *D. discoideum*
39 Δ *sey1* the formation of the ER-associated compartment harboring the bacterial pathogen
40 *Legionella pneumophila* was also impaired. In the mutant amoebae, the ER was less
41 efficiently recruited to the “*Legionella*-containing vacuole” (LCV), the expansion of the
42 pathogen vacuole was inhibited at early stages of infection and intracellular bacterial growth
43 was reduced. In summary, our study establishes a role of *D. discoideum* Sey1 in ER
44 architecture, proteolysis, cell motility and intracellular replication of *L. pneumophila*.

45

46

47 **1 INTRODUCTION**

48 The endoplasmic reticulum (ER) is a pleiomorphic organelle composed of perinuclear
49 membrane sheets and interconnected tubules extending towards the cell periphery (Shibata *et*
50 *al.*, 2006, English *et al.*, 2009). This tubular network undergoes constant remodeling by

1
2
3 51 homotypic fusion of ER tubules. Numerous proteins are required to form and maintain this
4
5 52 dynamic ER network (Shibata *et al.*, 2009). Among them, the membrane-bound large GTPase
6
7 53 atlastin (ATL) has been shown to mediate the homotypic fusion between tubules, ensuing the
8
9 54 formation of three-way junctions and subsequent extensive reticulation of the ER network
10
11 55 (Hu *et al.*, 2009, Orso *et al.*, 2009). In mammals, three ATL paralogs (ATL1-3) are
12
13 56 selectively produced in different tissues. ATLs are highly conserved during evolution with
14
15 57 only one single ortholog produced in yeast, plants or the amoeba *Dictyostelium discoideum*
16
17 58 (named Sey1 in these different organisms) (Chen *et al.*, 2011, Anwar *et al.*, 2012, Zhang *et*
18
19 59 *al.*, 2013, Steiner *et al.*, 2017). ATLs share a similar domain organization comprised of an N-
20
21 60 terminal GTPase and a three-helix bundle (3HB), followed by two closely spaced predicted
22
23 61 transmembrane (TM) segments and a C-terminal tail (CT). The role of ATLs in ER network
24
25 62 formation is emphasized by the observation that mutations in the ATL genes were detected in
26
27 63 the human neurological disorders hereditary spastic paraplegia (HSP) and hereditary sensory
28
29 64 neuropathy (HSN), which are characterized by severe ER morphological defects (Salinas *et*
30
31 65 *al.*, 2008, Guelly *et al.*, 2011, Fink, 2013, Fischer *et al.*, 2014, O'Donnell *et al.*, 2018).
32
33 66 Furthermore, ATL gene deletion and overexpression of dominant-negative mutants result in
34
35 67 defects of ER network formation (Rismanchi *et al.*, 2008, Hu *et al.*, 2009, Wang *et al.*, 2016,
36
37 68 Zhao *et al.*, 2016).

38
39
40 69 Structural and biochemical studies indicate that upon GTP binding, the GTPase domains of
41
42 70 ATL from two distinct ER tubules can form trans-homodimers, thus promoting membrane
43
44 71 contact and fusion (Bian *et al.*, 2011, Byrnes *et al.*, 2011). The fusogenic properties of ATLs
45
46 72 have been molecularly detailed by *in vitro* membrane fusion studies (Orso *et al.*, 2009, Bian *et*
47
48 73 *al.*, 2011, Anwar *et al.*, 2012, Kim *et al.*, 2017) and crystal structure analysis (Bian *et al.*,
49
50 74 2011, Byrnes *et al.*, 2011, Liu *et al.*, 2012, Byrnes *et al.*, 2013, Liu *et al.*, 2015). In addition to
51
52 75 ER dynamics, ATLs contribute to other cellular processes including lipid droplet biogenesis
53
54
55
56
57
58
59
60

1
2
3 76 (Klemm *et al.*, 2013), mitochondrial lipid exchange (Voss *et al.*, 2012), membrane tethering
4
5 77 (Krols *et al.*, 2018, Niu *et al.*, 2019), endosomal transport (Stefano *et al.*, 2015), inner nuclear
6
7 78 membrane protein insertion (Pawar *et al.*, 2017), and selective autophagy (Liang *et al.*, 2018,
8
9 79 Chen *et al.*, 2019).

10
11
12 80 Owing to numerous convenient genetic and biochemical tools, the amoeba *Dictyostelium*
13
14 81 *discoideum* has been widely used as a model organism to study eukaryotic cell biology and
15
16 82 host-pathogen interactions (Cardenal-Munoz *et al.*, 2017, Swart *et al.*, 2018). The phagocytic
17
18 83 amoebae can engulf and digest bacteria as nutritional sources. However, some pathogenic
19
20 84 bacteria avoid the degradative functions of *D. discoideum* and replicate inside this host cell.
21
22 85 For instance, *Legionella pneumophila*, the causative agent of a severe pneumonia in humans
23
24 86 termed Legionnaires' disease, induces the formation of a replication-permissive membrane-
25
26 87 bound compartment called "Legionella-containing vacuole" (LCV) in the amoeba (Swart *et*
27
28 88 *al.*, 2018).

29
30
31
32
33 89 The LCV biogenesis mechanism is comparable in human macrophages and amoeba
34
35 90 (Gomez-Valero *et al.*, 2011, Al-Quadan *et al.*, 2012), and relies on the delivery of more than
36
37 91 300 different "effector" proteins into host cells by the bacterial Icm/Dot (Intracellular
38
39 92 multiplication/defective organelle trafficking) type IV secretion system (T4SS). These
40
41 93 effectors target and control key host cell processes including vesicular trafficking in the
42
43 94 endocytic, secretory and retrograde pathways, lipid metabolism, translation, transcription, and
44
45 95 apoptosis (Isberg *et al.*, 2009, Asrat *et al.*, 2014, Finsel *et al.*, 2015, Personnic *et al.*, 2016,
46
47 96 Barlocher *et al.*, 2017, Steiner *et al.*, 2018a, Swart *et al.*, 2020a). The hijacking of host cell
48
49 97 functions notably leads to the recruitment of ER-derived vesicles (Kagan *et al.*, 2004), as well
50
51 98 as rough ER to LCVs (Swanson *et al.*, 1995, Robinson *et al.*, 2006, Weber *et al.*, 2014b,
52
53 99 Weber *et al.*, 2018). The ER associating with LCVs might provide structural elements for
54
55
56
57
58
59
60

1
2
3 100 pathogen vacuole formation and expansion, nutrients for intracellular growth, and/or
4
5 101 camouflage from host cell defenses (Sherwood *et al.*, 2016).

6
7 102 ATL3 and Sey1 have been identified by proteomics in intact LCVs purified from *L.*
8
9 103 *pneumophila*-infected macrophages or *Dictyostelium*, respectively (Hoffmann *et al.*, 2014).
10
11 104 Recently, we validated the presence of ATL3/Sey1 on LCVs, and we revealed a functional
12
13 105 role of this large GTPase for LCV formation (Steiner *et al.*, 2017). However, these studies
14
15 106 were limited to an analysis of infected *D. discoideum* or isolated LCVs upon overproduction
16
17 107 of a dominant negative Sey1 mutant, hampering further comprehensive studies. In order to
18
19 108 assess the role of Sey1 for cellular processes and host-pathogen interactions, we adopted a
20
21 109 genomic deletion strategy. In the present study, we uncovered the morphological and
22
23 110 functional consequences of Sey1 genetic inactivation in *Dictyostelium* and further detailed
24
25 111 Sey1 function(s) in the formation and expansion of the *Legionella* replicative vacuole.
26
27
28
29
30
31
32

33 113 **2 RESULTS**

34 114 **2.1 Construction and basic characterization of *D. discoideum* Δ sey1 cells**

35
36 115 The only atlastin protein in *D. discoideum* is termed Sey1 (Steiner *et al.*, 2017). To analyze
37
38 116 the function of Sey1, the corresponding gene was disrupted by insertion of the blasticidin
39
40 117 selection marker by double homologous recombination (Figure 1a). This insertion left only a
41
42 118 residual protein of 148 amino acids without any Sey1 functional domains. Several
43
44 119 independent clones were analyzed and displayed identical phenotypes, which were
45
46 120 complemented by transfection with the *sey1* coding sequence (see hereafter and data not
47
48 121 shown).
49
50
51
52
53

54 122 When attached to standard plastic cell culture dishes, *D. discoideum* lacking Sey1 (Δ sey1)
55
56 123 showed heterogeneously enlarged cell-surface size compared to Ax3 parental cells (2.2 times
57
58 124 the normal median size; Figures 1b and 1c). Electric current exclusion measurements (CASY
59
60

1
2
3 125 analyzer) further confirmed that $\Delta sey1$ cells had a greater diameter heterogeneity than Ax3
4
5 126 cells (mean diameters of 10.24 μm or 9.51 μm , respectively; Figure 1d). The *sey1* mutant
6
7 127 amoebae were also frequently polynucleated (Figure 1e), suggesting a cytokinesis defect as
8
9 128 described in fission yeast mutants affecting the cortical ER structure (Zhang *et al.*, 2010).
10
11 129 Moreover, the relative growth rate of the $\Delta sey1$ strain was slightly reduced, and a plateau
12
13 130 phase was reached at a lower cell density compared to Ax3 cells (Figure 1f). Upon starvation,
14
15 131 aggregates and fruiting bodies were observed with genuine timing (Figure 1g). In summary,
16
17 132 *D. discoideum* deleted for the *sey1* gene is viable and, compared to the parental strain, slightly
18
19 133 enlarged and more frequently polynucleated, but develops largely normally. Moreover, the
20
21 134 $\Delta sey1$ mutant strain grows slightly slower in axenic liquid medium.
22
23
24
25
26
27
28

29 136 **2.2 *D. discoideum* lacking Sey1 shows aberrant ER morphology and dynamics**

30
31 137 Since atlastin GTPases participate in the formation of the tubular ER network in other
32
33 138 organisms, we examined the ER morphology in *D. discoideum* $\Delta sey1$ cells by confocal
34
35 139 microscopy. In Ax3 parental cells, the ER-resident enzyme protein disulfide isomerase (PDI)
36
37 140 localized both at the nuclear periphery and at interconnected ER tubules, which appeared to
38
39 141 be extended throughout the entire cell towards the cell periphery (Figure 2a). In contrast, most
40
41 142 $\Delta sey1$ cells showed clumps of PDI positive tubules at the cell periphery and a reduced
42
43 143 interconnected ER tubule network. This altered ER morphology was identical in fixed and
44
45 144 live cells producing the ER-resident reporter protein calnexin A-GFP (CnxA-GFP) (Figures
46
47 145 2b and 2c). Furthermore, ectopic production of GFP-Sey1 but not GFP-Sey1_K154A
48
49 146 (GTPase defective mutant) in $\Delta sey1$ cells restored a normal ER morphology (Figure S1a),
50
51 147 indicating that the GTPase activity of Sey1 is required to form and maintain a native ER
52
53 148 network.
54
55
56
57
58
59
60

1
2
3 149 Moreover, the ER-shaping protein reticulon (Rtnlc in *D. discoideum*), an interactor of
4
5 150 Sey1, localized to ER tubules (but not to the perinuclear ER) in Ax3 and Δ sey1 cells upon
6
7
8 151 overproduction of an N-terminal GFP fusion protein, GFP-Rtnlc (Figure S1b). The ER-
9
10 152 resident SNARE (soluble NSF attachment receptor) proteins Sec22b, Ufe1, and Use1
11
12 153 localized to ER tubules as well as the perinuclear ER in Ax3 and Δ sey1 cells upon
13
14
15 154 overproduction of the corresponding GFP fusion proteins (Figure S2). Taken together, Sey1 is
16
17 155 required to establish normal ER architecture, but appears dispensable for the correct
18
19 156 localization of Rtnlc and ER SNARE proteins.

21
22 157 The ER network is a highly dynamic structure, wherein tubules are constantly branching
23
24 158 and fusing with each other (Schwarz *et al.*, 2016). To determine whether the absence of Sey1
25
26 159 might affect ER tubule dynamics, *D. discoideum* cells producing GFP-calnexin were analyzed
27
28
29 160 by time-lapse video microscopy. While in the parental Ax3 strain, GFP-calnexin-positive ER
30
31 161 tubules showed vivid dynamics, in live Δ sey1 cells, GFP-calnexin-labeled nodular clumps
32
33 162 were observed, which were mostly static. However, some faintly labeled ER tubules localized
34
35
36 163 between the nucleus and the cell periphery and showed dynamics similar to that of Ax3 cells
37
38 164 (Figure 2c, and Movies S1 and S2). These results indicate that tubule fusion and branching
39
40 165 still occur in Δ sey1 cells, however, to a much smaller extent.

42
43 166 Additional fluorescence microscopy analysis revealed that the morphology and distribution
44
45 167 of other intracellular compartments was not altered in Δ sey1 cells, and the architecture and
46
47 168 dynamics of the microtubule cytoskeleton was fully conserved in the mutant cells (Figure S3,
48
49
50 169 and Movies S3 and S4). Most importantly with regard to the functional analyses presented
51
52 170 hereafter, the overall structure of endocytic compartments appeared unaffected in *D.*
53
54 171 *discoideum* Δ sey1 (Figure S3), and the subcellular distributions of PtdIns(3)P and PtdIns(4)P,
55
56
57 172 hallmark phosphoinositide lipids of the endocytic and secretory pathway, respectively,
58
59 173 appeared normal (Figures S4a and S4b). These conclusions were further supported by
60

1
2
3 174 transmission electron microscopy (TEM) analysis which revealed no additional ultrastructural
4
5 175 defects in $\Delta sey1$ cells besides the aberrant ER morphology observed by optical microscopy
6
7
8 176 (Figure 2d). Taken together, the *D. discoideum* $\Delta sey1$ strain exhibits an aberrant ER tubule
9
10 177 network characterized by clumps of PDI- and calnexin-positive tubules, but otherwise appears
11
12 178 largely normal regarding cell organelle and cytoskeleton architecture and dynamics.
13
14
15 179

17 180 **2.3 *D. discoideum* $\Delta sey1$ cells are impaired for growth on bacterial lawns**

19 181 The reduced growth rate of $\Delta sey1$ cells in axenic liquid medium prompted us to examine their
20
21 182 endocytic capacities. *D. discoideum* feeds on liquid medium by macropinocytosis. To
22
23 183 evaluate this process, cells were incubated with fluorescent dextran for different periods of
24
25 184 time, and uptake was measured by flow cytometry analysis. Dextran uptake occurred at a
26
27 185 normal rate in $\Delta sey1$ cells, excluding that nutrient absorption is the growth-limiting step
28
29 186 (Figure 3a). In *D. discoideum*, lysosomes mature into post-lysosomes, which eventually fuse
30
31 187 with the plasma membrane and release their contents to the outside of the cells by exocytosis.
32
33 188 In $\Delta sey1$ cells, the rate of exocytosis of fluorescent dextran showed a moderate but significant
34
35 189 increase (51.3% of initial fluorescence retained after a chase period of 80 min in $\Delta sey1$ cells
36
37 190 compared to 66.1% in Ax3 cells) (Figure 3b).
38
39
40
41
42

43 191 *D. discoideum* can ingest other sources of nutrients (e.g. bacteria) by phagocytosis.
44
45 192 Surprisingly, $\Delta sey1$ cells could hardly grow on lawns of live (or even heat-killed) *Klebsiella*
46
47 193 *pneumoniae*, unless the mutant strain was complemented by plasmid-borne GFP-Sey1 and
48
49 194 myc-tagged Sey1 (Figures 3c and S5a). In contrast, the ectopic production of GFP-Sey1 in the
50
51 195 parental Ax3 strain did not affect its growth on a *K. pneumoniae* lawn. The growth defect of
52
53 196 $\Delta sey1$ was also observed with other bacterial strains, including *Escherichia coli* B/r and to a
54
55 197 lesser extent with *Bacillus subtilis* and *Micrococcus luteus* (Figure 3d). Thus, the growth
56
57
58
59
60

1
2
3 198 defect of *D. discoideum* $\Delta sey1$ occurs on lawns of different bacteria and is not restricted to
4
5 199 particular Gram-negative or Gram-positive bacteria.

6
7 200 To grow on bacteria, *D. discoideum* has to bind, internalize, kill, and finally digest the
8
9 201 bacterial cells. Interestingly, $\Delta sey1$ cells showed normal uptake of bacteria (*K. pneumoniae*)
10
11 202 and fluorescent beads (Figures 3e and 3f), excluding any major defects in particle
12
13 203 binding/recognition and uptake. Furthermore, identical bacteria killing efficiencies were
14
15 204 observed for Ax3 and $\Delta sey1$ cells (Figure 3g). In summary, compared to the parental strain,
16
17 205 $\Delta sey1$ cells show similar capacities for macropinocytosis, phagocytosis and exocytosis, but
18
19 206 are severely impaired for growth on lawns formed by a range of bacteria. Together these
20
21 207 results suggest that defective digestive functions might account for the growth defects of
22
23 208 $\Delta sey1$ cells.
24
25
26
27
28
29
30

31 210 **2.4 Lysosomal enzymes are hyper-secreted by $\Delta sey1$ cells**

32
33 211 To evaluate the digestion of bacteria by *D. discoideum* $\Delta sey1$, we first measured the activity
34
35 212 of lysozymes, a family of enzymes responsible for the degradation of bacterial cell wall
36
37 213 peptidoglycans (Lamrabet *et al.*, 2020). Two complementary assays revealed that $\Delta sey1$ cells
38
39 214 exhibited only 75% of the intracellular activity of lysozymes measured in Ax3 cells (Figure
40
41 215 4a). Since exocytosis is increased in $\Delta sey1$ cells (Figure 3b), we hypothesized that lysosomal
42
43 216 enzymes might be hyper-secreted, consequently decreasing their intracellular pool and
44
45 217 impairing degradative functions of the lysosomes. To test this hypothesis, we measured the
46
47 218 enzymatic activities of several lysosomal enzymes in cell and culture medium fractions
48
49 219 separated after cultivation for 24 h. A higher percentage of α -mannosidase, cathepsin D
50
51 220 (CtsD), and N-acetyl-glucosaminidase was secreted by $\Delta sey1$ compared to Ax3 cells, while
52
53 221 the secretion of acid phosphatase was the same (Figures 4b and S5b). This secretion
54
55 222 phenotype was largely reversed by the ectopic production of GFP-Sey1 (Figure 4b).
56
57
58
59
60

1
2
3 223 In addition, we noticed that hypersecretion of lysosomal enzymes was associated with
4
5 224 reduced total activities of α -mannosidase and CtsD inside the cells (Figure S5c). This
6
7 225 decrease was caused by lower amounts of cellular lysosomal enzymes and not by reduction of
8
9 226 their hydrolytic capacities when intracellularly retained. This was verified for CtsD by
10
11 227 Western blot of whole cell lysates with an anti-CtsD antibody. Accordingly, in $\Delta sey1$ cells, a
12
13 228 reduced amount of CtsD was observed in cell lysates, and this was partially compensated by
14
15 229 ectopic production of GFP-Sey1 (Figures 4c and 4d).

16
17
18
19 230 We also noticed that the apparent molecular weight of CtsD in $\Delta sey1$ cells corresponds to
20
21 231 the mature form of this enzyme (Figure 4c) (Journet *et al.*, 1999), suggesting that post-
22
23 232 translational protein modifications occur normally in $\Delta sey1$ cells. This was further confirmed
24
25 233 by the analysis of a highly glycosylated reporter protein, contact-site A (CsA) fused to
26
27 234 transmembrane and cytoplasmic domains of SibA (Froquet *et al.*, 2012). This CsA-SibA
28
29 235 chimeric protein showed the expected N- and O-glycosylation patterns in $\Delta sey1$ cells,
30
31 236 reflecting a preserved genuine glycosylation process (Figure S5d).

32
33
34
35 237 Moreover, the acidification of endocytic compartments, which is required for optimal
36
37 238 function of lysosomal enzymes, occurred at normal rates in $\Delta sey1$ cells, excluding any
38
39 239 enzymatic activity defects due to non-optimal pH of degradative compartments (Figure S5e).
40
41 240 Finally, total protein degradation in phagosomes was directly assessed by measuring
42
43 241 proteolysis of DQ Green-BSA-coated beads at 1 h after cellular uptake. This assay revealed a
44
45 242 10% reduction of proteolysis in $\Delta sey1$ cells (Figure 4e). Together, these observations indicate
46
47 243 that the intracellular retention of lysosomal enzymes is impaired in $\Delta sey1$ cells, consequently
48
49 244 likely reducing the hydrolytic processing of nutrients required for optimal growth of the
50
51 245 amoeba.

52
53
54
55 246

56 57 58 59 247 **2.5 *D. discoideum* lacking *sey1* shows defective cell motility**

60

1
2
3 248 Upon growth on bacterial lawns, *D. discoideum* cells leave “grazed” regions and move
4
5 249 towards more nutritive areas. To assess whether in addition to the impaired lysosomal
6
7
8 250 degradation, a reduced cell motility could contribute to the growth defect of Δ *sey1* cells,
9
10 251 random movement of individual cells seeded on a glass substrate in culture medium was
11
12 252 recorded by time-lapse confocal microscopy (Figure 5a). Mutant Δ *sey1* cells showed a
13
14 253 markedly reduced motility with a maximum distance from the initial position (D-max) of 23.0
15
16 $\pm 8.2 \mu\text{m}$ compared to $97.4 \pm 21.4 \mu\text{m}$ for the Ax3 cells (Figure 5b). The ectopic production
17 254
18 of GFP-Sey1 in Δ *sey1* cells partially restored motility (D-max = $68.6 \pm 22.5 \mu\text{m}$), in contrast
19 255
20 to the GTPase defective mutant GFP-Sey1_K154A, which had almost no effect (D-max =
21 256
22 $36.6 \pm 15.9 \mu\text{m}$). Moreover, while GFP-Sey1 did not affect the motility of Ax3 cells, the
23 257
24 GFP-Sey1_K154A mutant protein strongly inhibited their motility (D-max = $51.5 \pm 19.0 \mu\text{m}$),
25 258
26 indicating that the GTPase activity and/or dimerization of Sey1 is required for protein
27 259
28 function, and consequently, cell motility. Since Δ *sey1* cells exhibited no major alteration in
29 260
30 the organization of F-actin cellular protrusions (Figure S4c), other key players in cellular
31 261
32 motility are likely affected by Sey1 deletion. In summary, dependent on its GTPase activity,
33 262
34 Sey1 regulates the motility of *D. discoideum*.
35 263
36
37
38
39
40
41
42

265 **2.6 Sey1 contributes to ER homeostasis in stressed cells**

43 266
44
45 267
46
47
48
49
50 268
51
52 269
53
54
55 270
56
57 271
58
59 272
60

Atlastins in mammalian cells and RDH3 in plants have been shown to participate in the ER stress response (Lai *et al.*, 2014, Liang *et al.*, 2018, Chen *et al.*, 2019, Niu *et al.*, 2019). To test whether Sey1 adopts similar functions in *D. discoideum*, Δ *sey1* cells were incubated with tunicamycin (TN), a compound which induces ER stress and triggers the unfolded protein response (UPR) pathway (Dominguez-Martin *et al.*, 2018a, Dominguez-Martin *et al.*, 2018b). After 24 h of treatment the viability of Δ *sey1* was only slightly reduced compared to Ax3 cells (Figure 6a). However, this difference was dramatically amplified after 48 h and 72 h. After 48

1
2
3 273 h, only 21.5% $\Delta sey1$ cells were alive compared to 69.2% Ax3 cells, and at 72 h the difference
4
5 274 was also more than 3-fold. Phase contrast microscopy observations at 48 h further confirmed
6
7
8 275 these results (Figure 6b).

9
10 276 Interestingly, the viability difference between $\Delta sey1$ and the parental Ax3 strain was
11
12 277 dependent on the TN dose (Figure 6c). The viability of $\Delta sey1$ cells dropped to 45.9% at 125
13
14 278 ng/mL TN and reached a minimum of 20.2% viable cells at 1 $\mu\text{g/mL}$ TN. In contrast, Ax3
15
16 279 parental cells as well as $\Delta sey1$ cell ectopically producing RFP-Sey1 showed only a mild
17
18 280 reduction in viability (67.7% and 61.1% viable cells, respectively) even at the highest
19
20 281 concentration of TN tested (1.5 $\mu\text{g/mL}$). Thus, $\Delta sey1$ cells manage to readily adapt to short-
21
22 282 term ER stress, but exhibit strikingly reduced capacities to cope with prolonged ER stress.

23
24
25 283 To restore cellular homeostasis upon ER stress, cells increase protein degradation rates by
26
27 284 several mechanisms, including the ubiquitin-dependent ERAD (ER-associated degradation)
28
29 285 pathway and macroautophagy (hereafter referred to as autophagy) (Almanza *et al.*, 2019). To
30
31 286 assess a role for Sey1 in ERAD, we first tested the production of CdcD (ERAD protein
32
33 287 homologous to human VCP/p97 and yeast Cdc48) in response to TN (Figure 6d and 6e). In
34
35 288 agreement with published results (Dominguez-Martin *et al.*, 2018b), CdcD production
36
37 289 increased in Ax3 cells upon addition of TN for 24 h. A similar induction was observed in
38
39 290 $\Delta sey1$ cells; however, the basal production of CdcD in untreated cells was higher in $\Delta sey1$
40
41 291 than in Ax3 cells. This result might reflect a constitutive activation of the ERAD pathway in
42
43 292 mutant cells. In contrast, the basal production of PDI, a multifunctional ER-resident redox
44
45 293 chaperone, was not enhanced in resting $\Delta sey1$ cell, whereas TN treatment resulted in identical
46
47 294 induction of PDI production in $\Delta sey1$ and Ax3 cells, as expected for a treatment known to
48
49 295 augment protein folding capacities (Figure 6d and 6e). In summary, compared to the parental
50
51 296 Ax3 strain $\Delta sey1$ cells are more sensitive to ER stress.

52
53
54
55
56
57
58
59
60 297

2.7 Intracellular replication and killing of *L. pneumophila* in Δ *sey1* cells

Intracellular replication of *L. pneumophila* occurs in ER-associated LCVs and implicates Sey1 (Steiner *et al.*, 2017). To test intracellular growth of *L. pneumophila* in *D. discoideum* Δ *sey1* cells, we used mCherry-producing bacteria and quantified fluorescence intensity (RFU) as well as the number of colony-forming units (CFU) (Figures 7a and S6a). In both assays, wild-type *L. pneumophila* showed a severe growth defect upon replication in Δ *sey1* cells. On the other hand, the *L. pneumophila* Δ *icmT* mutant strain was unable to replicate in the *D. discoideum* Ax3 or Δ *sey1* strain (Figure 7a), and killing (or survival) of Δ *icmT* bacteria was not different in *D. discoideum* Δ *sey1* compared to the parental strain Ax3 (Figure 7b). Taken together, *L. pneumophila* replicates less efficiently in Δ *sey1* compared to the parental strain, and hence, Sey1 promotes intracellular replication of *L. pneumophila*.

2.8 Recruitment of rough ER to LCVs is impaired in *D. discoideum* Δ *sey1* cells

Given the various defects of *D. discoideum* Δ *sey1* cells in ER morphology and dynamics, we sought to assess LCV formation in the mutant amoebae. In order to obtain high-resolution images of LCVs in *D. discoideum* Ax3 and Δ *sey1* cells, we used regular TEM (Figure 7c). Upon infection with wild-type *L. pneumophila*, rough ER was observed at 2 h p.i. and 8 h p.i. around LCVs in *D. discoideum* Ax3 and in Δ *sey1* cells producing plasmid-borne GFP-Sey1, but not in Δ *sey1* mutant cells. No ER accumulated around vacuoles harboring the avirulent *L. pneumophila* Δ *icmT* in any of these *D. discoideum* strains at any time, as has been observed previously with amoebae producing dominant-negative GFP-Sey1_K154A (Steiner *et al.*, 2018b). In summary, in agreement with the severe defect of Δ *sey1* cells regarding ER morphology and dynamics, LCVs harboring wild-type *L. pneumophila* are not decorated with rough ER in the mutant amoebae.

323 **2.9 PtdIns(4)P-positive LCVs in *D. discoideum* Δ *sey1* acquire ER less robustly**

324 Next, we assessed LCV formation by confocal microscopy using dually labeled *D.*
325 *discoideum* Ax3 or Δ *sey1* producing the PtdIns(4)P/LCV probe P4C-mCherry and the ER
326 marker calnexin-GFP. Compared to the uninfected dually labeled Ax3 strain, in Δ *sey1* cells
327 the ER was disorganized, fragmented and showed a vesicular organization (Figures 2b and
328 S6b). This defective ER morphology was retained in *L. pneumophila*-infected Δ *sey1* cells and
329 was particularly striking at early time points of infection (up to 8 h p.i.; Figure 8).

330 In general, LCVs formed by wild-type *L. pneumophila* in the Δ *sey1* mutant accumulated
331 less calnexin-positive ER than LCVs in the parental strain Ax3, in particular at early time
332 points during infection (2 h p.i.) (Figure 8a). These fluorescence microscopy observations
333 validate the TEM data (Figure 7c). In the Δ *sey1* as well as in the Ax3 parental strain, the ER
334 localized to LCVs not homogeneously but in a rather patchy manner. Moreover, the
335 PtdIns(4)P-positive limiting LCV membrane was formed in Δ *sey1* cells as well as the parental
336 strain, and remained clearly visible throughout the infection (2 h - 48 h p.i.) (Figures 8, S6c,
337 and S6d).

338 To quantify the recruitment of calnexin to PtdIns(4)P-positive LCVs in an unbiased and
339 high-throughput manner, we used imaging flow cytometry (IFC). To this end, we infected the
340 dually labeled *D. discoideum* strain producing P4C-mCherry and calnexin-GFP with mPlum-
341 producing *L. pneumophila* (Figure 8b). The IFC colocalization score (see Materials and
342 Methods) for the acquisition of calnexin-GFP to LCVs was then assessed. The calnexin-GFP
343 colocalization score on LCVs formed by wild-type *L. pneumophila* increased during early
344 time points of infection (1 h - 6 h p.i.) (Figure 8b), and was significantly lower in amoebae
345 lacking *Sey1*. The calnexin-GFP colocalization score on LCVs decreased at later time-points
346 (24 h - 48 h p.i.; Figure S6e). Finally, calnexin-GFP did not colocalize on Δ *icmT*-containing
347 vacuoles in neither Ax3 or Δ *sey1* cells (data not shown), confirming that these LCVs do not

1
2
3 348 acquire ER (Weber *et al.*, 2014b, Steiner *et al.*, 2017). In summary, quantitative data from
4
5 349 IFC confirmed the confocal microscopy observations that Sey1 promotes the acquisition of
6
7
8 350 ER by LCVs harboring wild-type *L. pneumophila*.

9
10 351 Following the same procedure, we also assessed the time-dependent colocalization score of
11
12 352 P4C-mCherry on LCVs by IFC. The IFC colocalization score of P4C-mCherry on LCVs
13
14 353 formed by wild-type *L. pneumophila* increased during early time points of infection (1 h - 6 h
15
16 354 p.i.) (Figure 8b), while it decreased at later time points (24 h - 48 h p.i.) (Figure S6e). There
17
18
19 355 was almost no difference in the P4C-mCherry colocalization score between infected *D.*
20
21 356 *discoideum* Ax3 and Δ *sey1*. Hence, Sey1 appears dispensable for the acquisition of
22
23 357 PtdIns(4)*P* to the LCV membrane. Finally, P4C-mCherry was not observed on vacuoles
24
25 358 formed by Δ *icmT* mutant bacteria (data not shown), confirming that these LCVs do not
26
27
28 359 undergo PI conversion and are not decorated with PtdIns(4)*P* (Weber *et al.*, 2014a, Steiner *et*
29
30 360 *al.*, 2017). In summary, while the accumulation of calnexin-positive ER on LCVs in *D.*
31
32 361 *discoideum* is dependent on Sey1, the acquisition of PtdIns(4)*P* at the limiting LCV
33
34 362 membrane occurs independently of Sey1.

35
36
37
38 363

39 40 364 **2.10 LCV expansion is delayed in *D. discoideum* Δ *sey1* cells**

41
42 365 A hallmark of LCV maturation is its expansion to accommodate a growing number of
43
44 366 vacuolar bacteria. Comparing the LCV expansion in *D. discoideum* Ax3 and Δ *sey1*, we found
45
46
47 367 that while in the parental strain the PtdIns(4)*P*-positive limiting LCV membrane expanded, in
48
49 368 Δ *sey1* cells the PtdIns(4)*P*-positive membrane remained rather tightly wrapped around the
50
51 369 bacteria at early time points (2 h - 16 h p.i.) and only later expanded (24 h - 48 h p.i.) (Figures
52
53 370 8c, S6c, and S6d). These results indicate that Sey1 indeed promotes the expansion of the
54
55 371 PtdIns(4)*P*-positive LCV membrane early during infection but appears dispensable at later
56
57
58 372 stages of infection. The quantification of the LCV area revealed that at 2 h - 16 h p.i., LCVs
59
60

1
2
3 373 in Δ *sey1* cells were approximately 1.5-fold smaller than in the parental strain (Figure 8d). At
4
5 374 later time points (24 h - 48 h p.i.), the expansion defect disappeared, suggesting that *Sey1*
6
7 375 deletion only delays early LCV expansion (Figures 8c, 8d, S6c, and S6d). Taken together,
8
9 376 infection of dually labeled *D. discoideum* producing the PtdIns(4)P/LCV probe P4C-mCherry
10
11 377 and the ER marker calnexin-GFP revealed that in *D. discoideum* lacking *Sey1* LCV expansion
12
13 378 is delayed early during infection. Hence, *Sey1* plays a crucial role for LCV maturation and
14
15 379 intracellular replication of *L. pneumophila*.
16
17
18
19
20
21

22 381 **3 DISCUSSION**

23 24 382 **3.1 *D. discoideum* Δ *sey1* amoebae show an abnormal ER architecture**

25
26 383 *D. discoideum* deleted for *Sey1* were shown here to display an abnormal ER network
27
28 384 morphology, with disorganized clumps of ER tubules at the cell periphery, as reported for
29
30 385 several organisms following ATL gene deletion (Rismanchi *et al.*, 2008, Hu *et al.*, 2009,
31
32 386 Wang *et al.*, 2016, Zhao *et al.*, 2016). This morphological defect was only rescued by
33
34 387 overexpression of *Sey1* with a functional GTPase domain, consistent with the well-
35
36 388 established ATL GTPase-dependent fusion of tubules leading to the formation of three-way
37
38 389 junctions within tubules to create the cortical ER mesh. Unexpectedly, some ER branching
39
40 390 still occurred in the absence of *Sey1*, indicating that *Sey1*-independent fusion events might
41
42 391 partially compensate the loss of *Sey1*, thus ensuring cell viability. An alternative fusion
43
44 392 pathway mediated by the ER SNAREs Ufe1p, Sec22p/Sec20p, Use1p and the tethering Dsl1
45
46 393 complex has been described in *S. cerevisiae* (Rogers *et al.*, 2014). Since *D. discoideum*
47
48 394 orthologs of these SNAREs still localized to the ER in the absence of *Sey1*, a similar
49
50 395 SNARE-based fusion process might exist in this amoeba.
51
52
53
54
55

56
57 396 The stabilization of ER tubules is dependent on reticulon (Rtn) and Yop1p/DP1/REEP
58
59 397 families of ER-shaping proteins that directly interact with ATLs (Hu *et al.*, 2009, Park *et al.*,
60

1
2
3 398 2010). The ER-network formation requires a finely tuned balance between ATL-dependent
4
5 399 tubule fusion and Rtn-mediated tubule curvature (Wang *et al.*, 2016). *D. discoideum*
6
7 400 expresses only one Rtn ortholog (Rtnlc), and inhibition of Rtnlc functions by its deletion or
8
9 401 overexpression had no obvious consequences on the shape of ER tubules (Figures S1b and
10
11 402 S2c). The absence of defects in Δ rtnlc cells is consistent with the normal ER network
12
13 403 morphology observed in Rtn1p and Rtn2p deleted yeast cells (Voeltz *et al.*, 2006). Moreover,
14
15 404 the loss of RTN4a/b in mouse embryonic fibroblasts induces a reduction of ER tubulation
16
17 405 (Jozsef *et al.*, 2014), and the overexpression of the reticulons results in tubule fragmentation
18
19 406 (Wang *et al.*, 2016, Espadas *et al.*, 2019). This discrepancy suggests that besides Rtnlc, other
20
21 407 ER-shaping proteins might stabilize tubules in *D. discoideum*. PSI-BLAST searches did not
22
23 408 reveal any *D. discoideum* orthologs of DP1/Yop1/REEP proteins, and therefore, Δ rtnlc cells
24
25 409 might advantageously allow the identification of new tubule curvature mechanisms or factors.
26
27
28
29
30

31 410

32 33 411 **3.2 *D. discoideum* Δ sey1 amoebae upregulate the UPR pathway**

34
35 412 In mammalian cells, deletion of ATLs has been shown to induce the UPR pathway to limit
36
37 413 ER stress due to the delay in ER exit of some cargo proteins (Niu *et al.*, 2019). Confirming
38
39 414 this observation, we show here that Sey1 deletion caused the overexpression of the ERAD
40
41 415 protein CdcC, indicative of a constitutively active UPR pathway. This possibly implies that
42
43 416 the ER morphological defects in Δ sey1 cells might interfere with proper cargo protein sorting
44
45 417 or folding in the ER. Interestingly, we observed that Δ sey1 cells were unable to cope with
46
47 418 prolonged ER stress induced by tunicamycin. Besides the ERAD pathway, autophagy and ER
48
49 419 phagy/reticulophagy have been shown to contribute to the cellular response to ER stress
50
51 420 (Smith *et al.*, 2017, Song *et al.*, 2018, Stolz *et al.*, 2019, Wilkinson, 2019, Wilkinson, 2020).
52
53 421 Hence, the selection of ER subdomains containing damaged or excess material is mediated by
54
55 422 several specific ER-phagy receptors including atlastin (ATL3) (Chen *et al.*, 2019). Further
56
57
58
59
60

1
2
3 423 studies will be required to assess whether autophagy and ER-phagy processes are altered in
4
5 424 $\Delta sey1$ cells.
6
7

8 425

9
10 426 **3.3 *D. discoideum* $\Delta sey1$ amoebae are defective for growth on bacterial lawns**

11
12 427 *D. discoideum* $\Delta sey1$ cells had a marked growth defect when fed on bacteria and, to a lesser
13
14 428 extent, on axenic liquid culture medium. Our results indicate that at least two cumulative
15
16 429 defects in proteolysis and cell motility might account for these defective growth rates. First,
17
18 430 we established that reduced proteolytic capacities in $\Delta sey1$ cells were correlated with
19
20 431 impaired intracellular retention of lysosomal enzymes due to increased lysosomal exocytosis
21
22 432 rates. In *D. discoideum*, lysosomes undergo several maturation steps to form post-lysosomes
23
24 433 which eventually become competent to fuse with the plasma membrane to expel their content.
25
26 434 Lysosomal exocytosis defects have been described in several *D. discoideum* mutants affecting
27
28 435 lysosomal maturation before lysosome exocytosis (Charette *et al.*, 2007, Charette *et al.*, 2008,
29
30 436 Carnell *et al.*, 2011). Since no noticeable lysosomal maturation defects were observed in
31
32 437 $\Delta sey1$ cells, a hypothetical ER-dependent step in the exocytosis process might be altered in
33
34 438 the absence of Sey1. For instance, the ER might provide key factors owing its close proximity
35
36 439 to lysosomes at membrane contact sites (MCS) (Phillips *et al.*, 2016). The morphological
37
38 440 defects of the peripheral ER network in $\Delta sey1$ cells might interfere with the formation, the
39
40 441 location or even the function of these ER-lysosome MCS.
41
42
43
44
45
46

47 442 The growth defect on bacterial lawns might also be amplified by the reduced cell motility
48
49 443 observed in $\Delta sey1$ cells. The ER network has been shown to maintain connections with the
50
51 444 actin and microtubule cytoskeletons, both required for cell motility. Several ER proteins, such
52
53 445 as CLIMP63, P180, REEP1, Sec61b, and STIM1 physically interact with microtubules (MTs)
54
55 446 (Klopfenstein *et al.*, 1998, Ogawa-Goto *et al.*, 2007, Grigoriev *et al.*, 2008, Park *et al.*, 2010,
56
57 447 Zhu *et al.*, 2018), whereas SYP73 recruits the actin cytoskeleton in *Arabidopsis* (Cao *et al.*,
58
59
60

1
2
3 448 2016). A number of studies indicate that the ER can assist the cytoskeleton during organelle
4
5 449 and cell motility. For instance, spastin, an ATPase with MT-severing activity regulating MT
6
7 450 dynamics, has been shown to bind atlastin and REEP1 (Evans *et al.*, 2006, Sanderson *et al.*,
8
9 451 2006, Lee *et al.*, 2009, Park *et al.*, 2010), and its depletion affects the motility of
10
11 452 Glioblastoma cells (Draberova *et al.*, 2011). Furthermore, in *Arabidopsis*, deletion of the
12
13 453 atlastin-related protein RDH3 prevents ER streaming during cell expansion (Stefano *et al.*,
14
15 454 2014). Accordingly, the altered ER morphology of Δ *sey1* cells might hamper the proper
16
17 455 mobilization of ER tubules to physically assist the cytoskeleton during cell migration.

18
19
20
21 456 In the context of host-pathogen interactions, phagocytes infected with *L. pneumophila*
22
23 457 were impaired for cell and organelle motility (Rothmeier *et al.*, 2013, Swart *et al.*, 2020b). A
24
25 458 family of RCC1 repeat containing *L. pneumophila* effectors has been shown to activate the
26
27 459 small GTPase Ran, and consequently, stabilize MTs and promote cell and organelle motility.
28
29 460 It is unknown whether *L. pneumophila* has evolved strategies to interfere with ER-associated
30
31 461 motility functions.

32
33
34
35 462

36 37 463 **3.4 *D. discoideum* Δ *sey1* amoebae restrict growth of *L. pneumophila***

38
39 464 Inside eukaryotic host cells, the facultative intracellular bacterium *L. pneumophila* establishes
40
41 465 an ER-associated replication-permissive vacuole, the LCV. To this end, the pathogen employs
42
43 466 a multi-step process, including ATL3/Sey1-dependent ER recruitment (Steiner *et al.*, 2017).
44
45 467 Given the various defects of *D. discoideum* Δ *sey1* cells in ER morphology and dynamics, we
46
47 468 assessed intracellular replication and LCV formation in the mutant amoebae. Indeed, Δ *sey1*
48
49 469 cells restricted the intracellular growth of *L. pneumophila* but not the killing of an avirulent
50
51 470 mutant strain (Figures 7a and 7b). TEM and confocal microscopy analyses as well as IFC
52
53 471 revealed a disrupted ER morphology in Δ *sey1* cells and showed defective recruitment of ER
54
55 472 to LCVs, which was successfully complemented by plasmid-borne production of GFP-Sey1
56
57
58
59
60

1
2
3 473 (Figures 7c, 8a, and 8b). Moreover, confocal microscopy analysis using dually labeled *D.*
4
5 474 *discoideum* producing in parallel the PtdIns(4)*P*/LCV probe P4C-mCherry and the ER marker
6
7
8 475 calnexin-GFP revealed that the expansion of LCVs formed in Δ *sey1* cells was significantly
9
10 476 delayed (Figures 8c and 8d).

11
12 477 These findings are in agreement with previous observations using *D. discoideum*
13
14 478 producing a catalytically-inactive, dominant negative variant of Sey1 (Sey1_K154A), which
15
16
17 479 was found to inhibit intracellular replication of *L. pneumophila*, as well as the decoration with
18
19 480 ER, the expansion and the aggregation/fusion of LCVs (Steiner *et al.*, 2017, Steiner *et al.*,
20
21 481 2018a). In addition, the results reported in this study rule out off-target effects of
22
23
24 482 Sey1_K154A, such as the formation of heterodimers with large GTPases other than Sey1.
25
26 483 Indeed, the depletion by RNA interference of another large GTPase, the mitochondrial fission
27
28 484 factor DNMI1L (dynamin 1-like protein), has recently been shown to impair intracellular
29
30 485 replication of *L. pneumophila* (Escoll *et al.*, 2017).

31
32
33 486 The mechanism underlying the role of Sey1 for LCV expansion is unknown. Sey1-
34
35 487 catalyzed ER dynamics might promote the budding, trafficking and/or fusion of ER-derived
36
37
38 488 vesicles, which interact with the pathogen vacuole (Kagan *et al.*, 2002), and thus, contribute
39
40 489 to LCV maturation and expansion. Alternatively, the Sey1-catalyzed spatial vicinity of ER to
41
42 490 the PtdIns(4)*P*-positive pathogen vacuole might foster the formation of MCSs, which promote
43
44 491 lipid exchange and LCV expansion. Furthermore, our detailed analysis of the LCV maturation
45
46 492 kinetics by confocal microscopy indicated that the expansion of LCVs in the Δ *sey1* cells was
47
48 493 delayed only up to 16 h p.i. (Figures 8c and 8d). This defect appears to contribute to an
49
50
51 494 overall inhibition of intracellular replication of *L. pneumophila* in *D. discoideum* lacking Sey1
52
53 495 (Figure 7a). The replication defect appeared to be more pronounced in Δ *sey1* amoebae (~3-
54
55 496 fold decrease in replication) in comparison to the previously published defect caused by the
56
57
58 497 overproduction of the dominant negative Sey1 variant, Sey1_K154A (~2-fold decrease in
59
60

1
2
3 498 replication) (Steiner *et al.*, 2017). The reasons for a role of Sey1 in LCV expansion only at
4
5 499 rather early time points of infection and LCV maturation are unclear (Figures 8c, 8d, and S6).
6
7
8 500 Perhaps, fully functional ER architecture and dynamics are required only in the initial phase
9
10 501 to provide structural elements for LCV formation and expansion, nutrients for intracellular
11
12 502 growth, and/or protection from innate, host cell-autonomous defenses. Likely, the initial
13
14
15 503 phase of infection with a pathogen determines the outcome of the pathogen-host relationship,
16
17 504 i.e., that either the pathogen succeeds to establish a protective, replication-permissive niche,
18
19 505 or the host cell manages to kill the intruder.

20
21 506 In conclusion, in the present study we have characterized a number of phenotypes of *D.*
22
23 507 *discoideum* lacking Sey1. We showed that Δ *sey1* mutant amoebae are viable, exhibit
24
25 508 defective ER morphology and dynamics, reduced proteolytic processes and cell migration, as
26
27 509 well as impaired ER recruitment to LCVs, delay in pathogen vacuole expansion and reduced
28
29 510 intracellular replication of *L. pneumophila*. The successful generation of *D. discoideum* Δ *sey1*
30
31 511 mutant cells paves the way for further detailed characterization of the role of Sey1 in a variety
32
33 512 of cellular processes as well as for pathogen vacuole formation and maturation of different,
34
35 513 intracellular pathogens.
36
37
38
39
40
41

42 515 **4 EXPERIMENTAL PROCEDURES**

43 516 **4.1 Cell culture and *L. pneumophila* infections**

44
45 517 Detailed information on cell lines and bacterial strains used is reported in the Table S1. *D.*
46
47 518 *discoideum* strain Ax3 was grown at 22°C in HL5 medium or on lawns of live or heat-killed
48
49 519 bacteria as previously reported (Alibaud *et al.*, 2008). For infections with *L. pneumophila*, *D.*
50
51 520 *discoideum* Ax3 and Δ *sey1* mutant amoebae were cultivated in HL5 medium (ForMedium) at
52
53 521 23°C and transformed as previously described (Weber *et al.*, 2014a, Weber *et al.*, 2014b).
54
55 522 Transformation of two constructs in parallel was performed to obtain dually-fluorescent
56
57
58
59
60

1
2
3 523 strains. Geneticin (G418, 20 $\mu\text{g}/\text{mL}$) and hygromycin (50 $\mu\text{g}/\text{mL}$) was supplemented when
4
5 524 necessary.

6
7 525 *L. pneumophila* strains were grown for 3 days at 37°C on agar plates containing charcoal
8
9 526 yeast extract (CYE), buffered with *N*-(2-acetamido)-2-aminoethane sulfonic acid (ACES). For
10
11 527 infections, bacterial overnight cultures were prepared in ACES yeast extract (AYE) medium
12
13 528 at a starting OD₆₀₀ of 0.1 and were grown (21 h, 37°C) until early stationary phase (2×10^9
14
15 529 bacteria/mL). Chloramphenicol (Cam; 5 $\mu\text{g}/\text{mL}$) was supplemented when necessary.

16
17
18
19 530

20 21 531 **4.2 Cell surface and cell size analysis**

22
23 532 All cell lines were cultivated at low density a few days before analysis ($<10^6$ cells/mL). To
24
25 533 determine the surface of contact area between cells and culture plastic dishes, phase-contrast
26
27 534 images were analyzed using ImageJ. To measure cell size based on electric current exclusion
28
29 535 (CASY technology), cells were resuspended at a density of 5×10^5 cells/mL in culture
30
31 536 medium. After 2 h shaking, 200 μL cells were added to 10 mL CASYton solution and
32
33 537 analyzed using a CASY TTC instrument equipped with a 60 μm diameter capillary (OMNI
34
35 538 Life Science, Germany), kindly provided by Nicolas Talarek, IGMM/CNRS Montpellier.

36
37
38
39 539

40 41 540 **4.3 Plasmid construction**

42
43 541 All plasmids are described in Table S1. Rtnlc, Sec22b, Use1, Ufe1 coding sequences were
44
45 542 obtained by PCR from a cDNA library with the corresponding oligonucleotides (Table S2),
46
47 543 cloned in the indicated vectors and sequenced. Plasmids kindly provided by colleagues
48
49 544 include pCsA-SibA (P. Cosson; Centre Médical Universitaire, Geneva, Switzerland), as well
50
51 545 as RFP-2 \times FYVE and GFP-2 \times FYVE (J. King; University of Sheffield, Sheffield, UK).
52
53 546 Translational fusions of mRFPmars with wild-type Sey1 or the catalytically inactive mutant
54
55 547 (Sey1_K154A) were constructed by digestion of pBS001 or pNP108, respectively, with BglII
56
57
58
59
60

1
2
3 548 and SpeI. Subsequently, the ORFs of Sey1 or Sey1_K154A were cloned into the BglII and
4
5 549 SpeI sites of pDM318, yielding pBS003 and pBS004, respectively.
6
7
8 550

9 10 551 **4.4 Inactivation of *sey1* and *rtnlc***

11
12 552 A schematic representation of the strategies followed for genetic inactivation of *sey1* and
13
14 553 *rtnlc*, and PCR based identification is given in Figure S7. Δ *sey1* cells (*sey1* gene ID:
15
16 554 DDB_G0279823) were generated as follows. To construct the knockout vector (pFL1439),
17
18 555 the 5' fragment was amplified from genomic DNA with sense (OL1135) and antisense
19
20 556 (OL1136) oligonucleotides (from position 1 to 595 of the genomic DNA) and cloned into
21
22 557 pBlueScript vector (Stratagene, La Jolla, CA). The 3' fragment was obtained by PCR using
23
24 558 the GFP-Sey1 plasmid as template with sense (OL1137) and antisense (OL1138)
25
26 559 oligonucleotides (from position 2005 to 2862 of the genomic DNA) and cloned into
27
28 560 pBlueScript containing the 5' fragment. After sequencing, the knockout vector was completed
29
30 561 by inserting the blasticidin resistance cassette between the two 5' and 3' fragments. The
31
32 562 resulting plasmid was linearized (KpnI and NotI digestion) and electroporated into Ax3 cells
33
34 563 as reported (Alibaud *et al.*, 2003). Transformants were selected in presence of 10 μ g/mL
35
36 564 blasticidin. Individual colonies were tested by PCR to confirm *sey1* gene replacement.
37
38
39
40
41

42 565 Δ *rtnlc* cells (*rtnlc* gene ID: DDB_G0293088) were generated as follows. To obtain the
43
44 566 knockout vector (pFL1477), the 5' fragment was amplified from pFL1472 with sense
45
46 567 (OL1198) and antisense (OL1199) oligonucleotides (from position 192 to 584 of the genomic
47
48 568 DNA) and cloned into pBlueScript vector. The 3' fragment was obtained by PCR from
49
50 569 genomic DNA using sense (OL1200) and antisense (OL1201) oligonucleotides (from position
51
52 570 852 to 1243 of the genomic DNA) and cloned into pBlueScript containing the 5' fragment.
53
54 571 After sequencing, the knockout vector was completed by inserting the blasticidin resistance
55
56 572 cassette between the two 5' and 3' fragments. Ax3 cells were electroporated with the
57
58
59
60

1
2
3 573 linearized vector (KpnI and NotI digestion), and $\Delta rtnlc$ clones were selected as described
4
5 574 above for Sey1.
6
7
8 575

9 10 576 **4.5 Endocytosis, exocytosis, glycosidase and proteolytic activities**

11
12 577 Analysis of fluid phase (Alexa-Fluor-647-dextran; Molecular Probes) uptake/exocytosis,
13
14 578 phagocytosis of particles (YG-fluorescent 1- μ m latex beads; Polysciences) or GFP-producing
15
16
17 579 *K. pneumoniae* bacteria, was performed by flow cytometry as previously described (Lima *et*
18
19 580 *al.*, 2012) (BD FACSCanto II,bdbiosciences). All data were normalized to protein content.

20
21 581 Intracellular and secreted glycosidase activities were measured as previously described
22
23 582 (Froquet *et al.*, 2008, Le Coadic *et al.*, 2013). CtsD activity was analyzed by measuring the
24
25 583 fluorescence release of a specific fluorogenic substrate (Mca-Gly-Lys-Pro-Ile-Leu-Phe-Phe-
26
27 584 Arg-Leu-Lys(Dnp)-D-Arg-NH₂ [Mca = (7-methoxycoumarin-4-yl)acetyl; Dnp = dinitro-
28
29 585 phenyl]; BML-P145-0001, Enzo) with a microplate reader (Spark 20M, Tecan Life Sciences).

30
31 586 Lysozymes enzymatic activity in cell lysates was measured by the reduction of turbidity of
32
33 587 heat-killed *Micrococcus lysodeikticus* (Sigma) in suspension or on agarose plates as described
34
35 588 (Le Coadic *et al.*, 2013, Bodinier *et al.*, 2020). To measure intracellular proteolysis, 50 mg
36
37 589 carboxylate-modified microspheres, 2.0 μ m, blue fluorescent (365/415nm) (FluoSpheres,
38
39 590 Molecular Probes, Thermofisher) were incubated overnight with 1 mg DQ-Green-labeled
40
41 591 BSA (Invitrogen, Thermofisher) under continuous rotation. Coated beads were washed by
42
43 592 five cycles of low speed centrifugation and resuspension in culture medium. Cells were next
44
45 593 incubated with beads for 30 min, washed, and further incubated for 30 min. Intracellular
46
47 594 proteolysis of BSA released DQ-Green fluorescence (505/515 nm), and intrinsic fluorescence
48
49 595 of the beads (365/415nm) were measured by flow cytometry.
50
51
52
53
54
55

56 596

57 58 597 **4.6 Analysis of the UPR pathway**

59
60

1
2
3 598 To analyze cell viability upon tunicamycin (TN) treatment, cells were seeded at $1-2 \times 10^5$
4
5 599 cells/well on 24 wells tissue culture plates and treated with TN. At the indicated times, cells
6
7 600 were resuspended by pipetting, and propidium iodide was added for 10 min before flow
8
9 601 cytometry analysis.

10
11
12 602 Analysis of PDI, CdcD and EHD production was performed by Western blotting as
13
14 603 reported (Dominguez-Martin *et al.*, 2018b). Briefly, cells were first seeded at 10^6 cells/well
15
16 604 on 6-wells tissue culture plates. After incubation for 24 h with 1.5 $\mu\text{g}/\text{mL}$ TN, cells were
17
18 605 washed once in phosphate buffer, and lysed for 30 min on ice in RIPA lysis buffer (10 mM
19
20 606 Tris-HCl, pH 7.5, 150 mM NaCl, 0.5 mM EDTA, 0.5% NP-40, 0.05% SDS, protease
21
22 607 inhibitors) (100 $\mu\text{L}/\text{well}$). Protein concentrations were determined and adjusted before SDS
23
24 608 polyacrylamide electrophoresis and immunoblotting were performed as previously described
25
26 609 (Cornillon *et al.*, 2000). Proteins were revealed by ECL (Thermo Scientific, Courtaboeuf,
27
28 610 France) and a ChemiDoc MP imager (Bio-Rad, Marnes-la-Coquette, France) allowing signal
29
30 611 quantification (ImageQuant software).
31
32
33
34

35 612

36 37 613 **4.7 Immunofluorescence microscopy**

38
39 614 Antibodies used in this study are described in Table S3. Anti-p97 (CdcD) and Alexa-Fluor-
40
41 615 647-coupled anti-p80 antibodies were kindly provided by L. Eichinger (University of
42
43 616 Cologne, Cologne, Germany) and P. Cosson (Centre Médical Universitaire, Geneva,
44
45 617 Switzerland), respectively. Actin was stained with TRITC-labeled phalloidin (Sigma-
46
47 618 Aldrich). For immunofluorescence analysis of uninfected *D. discoideum*, cells were fixed and
48
49 619 processed as previously detailed (Dias *et al.*, 2013). Cells were observed with an inverted
50
51 620 Zeiss Axio Observer microscope or by confocal microscopy (either Leica SPE or Zeiss
52
53 621 Confocal ZEISS 880 with Fast Airyscan).
54
55
56
57

58 622
59
60

623 **4.8 Live cell imaging and analysis**

624 To analyze cell motility, cells were deposited on 35 mm glass bottom dish (Ibidi) in filtered
625 HL5 medium and imaged with a spinning disc Nikon Ti Andor CSU-W1 confocal microscope
626 every 30 s for 30 min. Films were processed by manual centroid tracking with the ImageJ
627 plugin MTrackJ. To analyze microtubule and calnexin dynamics, cells were attached to glass
628 coverslips in filtered HL5 medium for at least 30 min and overlaid with a 1 mm thin agarose
629 sheet before observation. Images were taken every second for 2 min with a confocal ZEISS
630 880 microscope equipped with Fast Airyscan detection.

631

632 **4.9 Intracellular growth and killing of *L. pneumophila* in *D. discoideum***

633 Intracellular replication of *L. pneumophila* JR32 and $\Delta icmT$ in *D. discoideum* Ax3 and $\Delta sey1$
634 mutant cells was analyzed by colony forming units (CFUs) as well as by increase in relative
635 fluorescent units (RFUs) following intravacuolar replication of mCherry-producing *L.*
636 *pneumophila* strains. To determine CFUs, GFP-producing *D. discoideum* Ax3 or $\Delta sey1$
637 amoebae were seeded at a density of 1×10^5 cells/mL in cell culture-treated 96-wells plates
638 (VWR) and cultivated at 23°C in HL5 medium containing geneticin (G418, 20 μ g/mL).
639 Afterwards, the amoebae were infected (MOI 1) with early stationary phase *L. pneumophila*
640 JR32 or $\Delta icmT$ constitutively producing mCherry, diluted in MB medium (Solomon *et al.*,
641 2000), centrifuged (450 g, 10 min, RT) and incubated for 1 h at 25°C. Subsequently, the
642 infected amoebae were washed 3 times with MB medium and incubated at 25°C for the time
643 indicated (96-wells plate was kept moist by addition of ddH₂O in surrounding wells). The
644 cells were lysed with 0.8% saponin (Sigma-Aldrich) for 10 min at RT, and dilutions were
645 plated on CYE agar plates containing Cam (5 μ g/mL) and incubated at 37°C for 3 days. CFUs
646 were assessed using an automated colony counter (CounterMat Flash 4000, IUL Instruments,
647 CounterMat software), and the number of CFUs (per mL) was calculated. Using the same

1
2
3 648 procedure, killing of mCherry-producing *L. pneumophila* $\Delta icmT$ (MOI 50) was assessed in
4
5 649 GFP-producing *D. discoideum* Ax3 or $\Delta sey1$. Following CFU counting, the percentage of
6
7
8 650 surviving bacteria (in relation to the initial bacteria number) was calculated for each time
9
10 651 point.

11
12 652 To determine increase in fluorescence derived from intracellular replication of mCherry-
13
14 653 producing *L. pneumophila*, GFP-producing *D. discoideum* Ax3 or $\Delta sey1$ amoebae were
15
16
17 654 seeded at a density of 1×10^5 cells/mL in cell culture-treated 96-wells plates (VWR) and
18
19 655 cultivated at 23°C in HL5 medium containing geneticin (G418, 20 $\mu\text{g}/\text{mL}$). The cells were
20
21 656 infected (MOI 1) with early stationary phase mCherry-producing *L. pneumophila* JR32,
22
23
24 657 diluted in MB medium, centrifuged (450 g, 10 min, RT) and incubated for 1 h at 25°C.
25
26 658 Afterwards, the infected amoebae were washed 3 times with fresh MB medium and incubated
27
28 659 at 25°C for the time indicated (96-wells plate was kept moist by addition of ddH₂O in
29
30 660 surrounding wells). Increase in mCherry fluorescence was assessed every 2 days using a
31
32
33 661 microtiter plate reader (Synergy H1, Biotek).

34
35 662

36 37 663 **4.10 Confocal microscopy of infected cells**

38
39 664 Infected *D. discoideum* amoebae were fixed and imaged by confocal microscopy. In short,
40
41
42 665 exponential phase *D. discoideum* Ax3 and $\Delta sey1$ amoebae producing calnexin-GFP and P4C-
43
44 666 mCherry were seeded in cell culture-treated 6-wells plates (VWR) at a density of 1×10^5
45
46 667 cells/mL or 2×10^5 cells/mL respectively, and cultured overnight at 23°C in HL5 medium
47
48 668 containing geneticin (G418, 20 $\mu\text{g}/\text{mL}$) and hygromycin (50 $\mu\text{g}/\text{mL}$). The cells were infected
49
50
51 669 (MOI 5) with mCerulean-producing *L. pneumophila* JR32 diluted in HL5, synchronized by
52
53
54 670 centrifugation (450 g, 10 min, RT) and incubated at 25°C for 1 h. Infected amoebae were then
55
56 671 washed 3 times with fresh HL5 and incubated at 25°C for the time indicated. Subsequently,
57
58 672 infected cells (including supernatant) were collected from the 6-wells plate, centrifuged (500
59
60

1
2
3 673 g, 5 min, RT) and fixed with 4% PFA (Electron Microscopy Sciences) for 30 min at RT.
4
5 674 Fixed cells were then washed twice with Soerensen phosphate buffer (SorC) (Malchow *et al.*,
6
7 675 1972), transferred to a 8-wells μ -slide dish (Ibidi) and embedded under a layer of PBS/0.5%
8
9 676 agarose.

10
11
12 677 The samples were imaged with a Leica TCS SP8 X CLSM (HC PL APO CS2, objective
13
14 678 63 \times /1.4–0.60 oil; Leica Microsystems) with a scanning speed of 400 Hz, bi-directional laser
15
16
17 679 scan and line accumulation equal 2. Pictures were acquired with a pinhole of 1.19 Airy Units
18
19 680 (AU) and with a pixel/voxel size close to the instrument's Nyquist criterion of 43 \times 43 \times 130 nm
20
21 681 (xyz). Images were deconvolved with Huygens professional version 19.10 software
22
23 682 (Scientific Volume Imaging, <http://svi.nl>) using the CMLE algorithm, set to 40 iterations and
24
25 683 quality threshold of 0.05. Z-stacks were finalized/exported using Imaris 9.5.0 software
26
27 684 (Bitplane).

28
29
30
31 685

32 33 686 **4.11 Imaging flow cytometry**

34
35 687 Processing of infected amoebae for imaging flow cytometry (IFC) was performed essentially
36
37 688 as described (Welin *et al.*, 2018). In short, *D. discoideum* Ax3 and Δ *sey1* mutant producing
38
39 689 calnexin-GFP and P4C-mCherry were seeded in T-75 flasks containing HL5 medium,
40
41 690 geneticin (G418, 20 μ g/mL) and hygromycin (50 μ g/mL), and infected (MOI 5) with mPlum-
42
43 691 producing *L. pneumophila* JR32 diluted in HL5 medium. The infection was synchronized by
44
45 692 centrifugation (450 g, 10 min, RT), and the cells were incubated for 1 h at 25°C. Infected cells
46
47 693 were then washed three times with HL5 and incubated at 25°C for the time indicated.
48
49 694 Afterwards, cells were collected, centrifuged (500 g, 5 min, RT) and fixed in 2% PFA for 90
50
51 695 min on ice. Fixed infected amoebae were washed twice in phosphate-buffered saline (PBS)
52
53 696 and resuspended in 20 μ L ice-cold PBS prior to IFC analysis.
54
55
56
57
58
59
60

1
2
3 697 Using an imaging flow cytometer (ImageStreamX MkII; Amnis), at least 5'000 cells were
4
5 698 acquired and analyzed with the IDEAS (v.6.2) software (Amnis). In short, infected amoebae
6
7 699 containing one intracellular *L. pneumophila* bacterium were gated and analyzed for
8
9 700 colocalization of GFP and mCherry (host) with mPlum produced by *L. pneumophila*
10
11 701 (minimum number of gated events specified in the figure legend). The software computes the
12
13 702 IFC colocalization score (bright detail similarity), which is the log-transformed Pearson's
14
15 703 correlation coefficient of the localized bright spots with a radius of 3 pixels or less in two
16
17 704 images, and is used to quantify relative enrichment of a marker on the LCV. Data analysis
18
19 705 was performed using GraphPad Prism. Regular two-way ANOVA followed by Bonferroni
20
21 706 post-hoc test was used to compare all samples between each other.
22
23
24
25

26 707

27 28 708 **4.12 Electron microscopy**

29
30 709 *L. pneumophila*-infected *D. discoideum* Ax3, Δ *sey1* producing GFP or Δ *sey1* producing GFP-
31
32 710 *Sey1* were fixed with 4% PFA and 0.1% glutaraldehyde in 0.1 M sodium cacodylate buffer
33
34 711 (pH 7.35) for 30 min at 4°C. Afterwards, the samples were treated sequentially with 2.5%
35
36 712 glutaraldehyde for 30 min, 1% OsO₄ for 1 h at 0°C, both in 0.1 M sodium cacodylate buffer
37
38 713 and 2% uranyl acetate in ddH₂O for 1 h at 4°C, followed by embedment in 2% Difco Noble
39
40 714 agar (BD Biosciences, Allschwil, Switzerland) in H₂O to form an immobilized pellet. An
41
42 715 increasing ethanol series (50%-100%) was then used to dehydrate the samples, which were
43
44 716 finally embedded in Epon/Araldite (Sigma-Aldrich). Contrast enhancement of ultrathin (50
45
46 717 nm) sections was done using Reynolds lead citrate. Processed samples were examined with a
47
48 718 CM100 transmission electron microscope (Thermo Fisher Scientific, Eindhoven, The
49
50 719 Netherlands) at an acceleration voltage of 80 kV using an Orius 1000 digital camera (Ametek
51
52 720 GmbH, Munich, Germany).
53
54
55
56
57

58 721

59
60

722 ACKNOWLEDGEMENTS

723 Confocal laser scanning microscopy and TEM was performed using equipment of the Center
724 of Microscopy and Image Analysis, University of Zurich (UZH), run by Andres Kaech and
725 Urs Ziegler. Imaging Flow Cytometry was performed at the Flow Cytometry Core Facility of
726 the Faculty of Medicine and Health Sciences, Linköping University, Linköping, Sweden.
727 Flow cytometry and microscopy analyses of uninfected cells were performed at the
728 Montpellier RIO imaging facility of the University of Montpellier, member of the national
729 infrastructure France-BioImaging, supported by the French National Research Agency (ANR-
730 10-INBS-04, “Investments for the future”). Work in the group of H.H. was supported by the
731 Swiss National Science Foundation (SNF; 31003A_175557), the Novartis Foundation for
732 Medical-Biological Research, and the OPO foundation. Work in the group of V.M. and F.L.
733 was supported by the Région Occitanie. A.W. was supported by grants from the Swedish
734 Society of Medicine (SLS-934829) and the Åke Wiberg Foundation. The funders had no role
735 in study design, data collection and analysis, decision to publish, or preparation of the
736 manuscript.

737

738 AUTHORS' CONTRIBUTION

739 H.H. and F.L. conceived the study and guided experiments. D.H., Be.S., A.W., Bi.S., A.L.S.
740 and F.L. designed and conducted experiments. V.M. provided funding. H.H. and F.L. wrote
741 the paper with input from all other authors.

742

743 CONFLICT OF INTEREST

744 The authors declare no conflict of interest.

745

746 REFERENCES

- 747 Al-Quadani, T., Price, C.T. and Abu Kwaik, Y. (2012). Exploitation of evolutionarily
748 conserved amoeba and mammalian processes by *Legionella*. *Trends in Microbiology* **20**,
749 299-306.
- 750 Alibaud, L., Cosson, P. and Benghezal, M. (2003). *Dictyostelium discoideum* transformation
751 by oscillating electric field electroporation. *BioTechniques* **35**, 78-80, 82-73.
- 752 Alibaud, L., Kohler, T., Coudray, A., Prigent-Combaret, C., Bergeret, E., Perrin, J., *et al.*
753 (2008). *Pseudomonas aeruginosa* virulence genes identified in a *Dictyostelium* host model.
754 *Cellular Microbiology* **10**, 729-740.
- 755 Almanza, A., Carlesso, A., Chintia, C., Creedican, S., Doultinos, D., Leuzzi, B., *et al.*
756 (2019). Endoplasmic reticulum stress signalling - from basic mechanisms to clinical
757 applications. *The FEBS Journal* **286**, 241-278.
- 758 Anwar, K., Klemm, R.W., Condon, A., Severin, K.N., Zhang, M., Ghirlando, R., *et al.* (2012).
759 The dynamin-like GTPase Sey1p mediates homotypic ER fusion in *S. cerevisiae*. *The*
760 *Journal of Cell Biology* **197**, 209-217.
- 761 Asrat, S., de Jesus, D.A., Hempstead, A.D., Ramabhadran, V. and Isberg, R.R. (2014).
762 Bacterial pathogen manipulation of host membrane trafficking. *Annual Review of Cell and*
763 *Developmental Biology* **30**, 79-109.
- 764 Bärlocher, K., Welin, A. and Hilbi, H. (2017). Formation of the *Legionella* replicative
765 compartment at the crossroads of retrograde trafficking. *Frontiers in Cellular and Infection*
766 *Microbiology* **7**, 482.
- 767 Bian, X., Klemm, R.W., Liu, T.Y., Zhang, M., Sun, S., Sui, X., *et al.* (2011). Structures of the
768 atlastin GTPase provide insight into homotypic fusion of endoplasmic reticulum
769 membranes. *Proceedings of the National Academy of Sciences of the United States of*
770 *America* **108**, 3976-3981.

- 1
2
3 771 Bodinier, R., Leiba, J., Sabra, A., Jauslin, T.N., Lamrabet, O., Guilhen, C., *et al.* (2020).
4
5 772 LrrkA, a kinase with leucine-rich repeats, links folate sensing with Kil2 activity and
6
7 773 intracellular killing. *Cellular Microbiology* **22**, e13129.
8
9
10 774 Byrnes, L.J., Singh, A., Szeto, K., Benveniste, N.M., O'Donnell, J.P., Zipfel, W.R. and
11
12 775 Sondermann, H. (2013). Structural basis for conformational switching and GTP loading of
13
14 776 the large G protein atlastin. *The EMBO Journal* **32**, 369-384.
15
16
17 777 Byrnes, L.J. and Sondermann, H. (2011). Structural basis for the nucleotide-dependent
18
19 778 dimerization of the large G protein atlastin-1/SPG3A. *Proceedings of the National*
20
21 779 *Academy of Sciences of the United States of America* **108**, 2216-2221.
22
23
24 780 Cao, P., Renna, L., Stefano, G. and Brandizzi, F. (2016). SYP73 Anchors the ER to the actin
25
26 781 cytoskeleton for maintenance of ER integrity and streaming in *Arabidopsis*. *Current*
27
28 782 *Biology* **26**, 3245-3254.
29
30
31 783 Cardenal-Munoz, E., Barisch, C., Lefrancois, L.H., Lopez-Jimenez, A.T. and Soldati, T.
32
33 784 (2017). When Dicty met Myco, a (not so) romantic story about one amoeba and its
34
35 785 intracellular pathogen. *Frontiers in Cellular and Infection Microbiology* **7**, 529.
36
37
38 786 Carnell, M., Zech, T., Calaminus, S.D., Ura, S., Hagedorn, M., Johnston, S.A., *et al.* (2011).
39
40 787 Actin polymerization driven by WASH causes V-ATPase retrieval and vesicle
41
42 788 neutralization before exocytosis. *The Journal of Cell Biology* **193**, 831-839.
43
44
45 789 Charette, S.J. and Cosson, P. (2007). A LYST/beige homolog is involved in biogenesis of
46
47 790 *Dictyostelium* secretory lysosomes. *Journal of Cell Science* **120**, 2338-2343.
48
49 791 Charette, S.J. and Cosson, P. (2008). Altered composition and secretion of lysosome-derived
50
51 792 compartments in *Dictyostelium* AP-3 mutant cells. *Traffic* **9**, 588-596.
52
53
54 793 Chen, J., Stefano, G., Brandizzi, F. and Zheng, H. (2011). Arabidopsis RHD3 mediates the
55
56 794 generation of the tubular ER network and is required for Golgi distribution and motility in
57
58 795 plant cells. *Journal of Cell Science* **124**, 2241-2252.
59
60

- 1
2
3 796 Chen, Q., Xiao, Y., Chai, P., Zheng, P., Teng, J. and Chen, J. (2019). ATL3 is a tubular ER-
4
5 797 phagy receptor for GABARAP-mediated selective autophagy. *Current Biology* **29**, 846-
6
7 798 855.
- 9
10 799 Cornillon, S., Pech, E., Benghezal, M., Ravanel, K., Gaynor, E., Letourneur, F., *et al.* (2000).
11
12 800 Phg1p is a nine-transmembrane protein superfamily member involved in *Dictyostelium*
13
14 801 adhesion and phagocytosis. *The Journal of Biological Chemistry* **275**, 34287-34292.
- 16
17 802 Dias, M., Blanc, C., Thazar-Poulot, N., Ben Larbi, S., Cosson, P. and Letourneur, F. (2013).
18
19 803 *Dictyostelium* ACAP-A is an ArfGAP involved in cytokinesis, cell migration and actin
20
21 804 cytoskeleton dynamics. *Journal of Cell Science* **126**, 756-766.
- 23
24 805 Dominguez-Martin, E., Hernandez-Elvira, M., Vincent, O., Coria, R. and Escalante, R.
25
26 806 (2018a). Unfolding the endoplasmic reticulum of a social amoeba: *Dictyostelium*
27
28 807 *discoideum* as a new model for the study of endoplasmic reticulum stress. *Cells* **7**, 56.
- 30
31 808 Dominguez-Martin, E., Ongay-Larios, L., Kawasaki, L., Vincent, O., Coello, G., Coria, R.
32
33 809 and Escalante, R. (2018b). IreA controls endoplasmic reticulum stress-induced autophagy
34
35 810 and survival through homeostasis recovery. *Molecular and Cellular Biology* **38**, e00054-
36
37 811 18.
- 39
40 812 Draberova, E., Vinopal, S., Morfini, G., Liu, P.S., Sladkova, V., Sulimenko, T., *et al.* (2011).
41
42 813 Microtubule-severing ATPase spastin in glioblastoma: increased expression in human
43
44 814 glioblastoma cell lines and inverse roles in cell motility and proliferation. *The Journal of*
45
46 815 *Neuropathology and Experimental Neurology* **70**, 811-826.
- 48
49 816 English, A.R., Zurek, N. and Voeltz, G.K. (2009). Peripheral ER structure and function.
50
51 817 *Current Opinion in Cell Biology* **21**, 596-602.
- 53
54 818 Escoll, P., Song, O.R., Viana, F., Steiner, B., Lagache, T., Olivo-Marin, J.C., *et al.* (2017).
55
56 819 *Legionella pneumophila* modulates mitochondrial dynamics to trigger metabolic
57
58 820 repurposing of infected macrophages. *Cell Host & Microbe* **22**, 302-316.
- 59
60

- 1
2
3 821 Espadas, J., Pendin, D., Bocanegra, R., Escalada, A., Misticoni, G., Trevisan, T., *et al.* (2019).
4
5 822 Dynamic constriction and fission of endoplasmic reticulum membranes by reticulon. *Nat*
6
7 823 *Commun* **10**, 5327.
8
9
10 824 Evans, K., Keller, C., Pavur, K., Glasgow, K., Conn, B. and Lauring, B. (2006). Interaction of
11
12 825 two hereditary spastic paraplegia gene products, spastin and atlastin, suggests a common
13
14 826 pathway for axonal maintenance. *Proceedings of the National Academy of Sciences of the*
15
16 827 *United States of America* **103**, 10666-10671.
17
18
19 828 Fink, J.K. (2013). Hereditary spastic paraplegia: clinico-pathologic features and emerging
20
21 829 molecular mechanisms. *Acta Neuropathology* **126**, 307-328.
22
23
24 830 Finsel, I. and Hilbi, H. (2015). Formation of a pathogen vacuole according to *Legionella*
25
26 831 *pneumophila*: how to kill one bird with many stones. *Cellular Microbiology* **17**, 935-950.
27
28
29 832 Fischer, D., Schabhuttli, M., Wieland, T., Windhager, R., Strom, T.M. and Auer-Grumbach,
30
31 833 M. (2014). A novel missense mutation confirms ATL3 as a gene for hereditary sensory
32
33 834 neuropathy type 1. *Brain* **137**, e286.
34
35
36 835 Froquet, R., Cherix, N., Birke, R., Benghezal, M., Cameroni, E., Letourneur, F., *et al.* (2008).
37
38 836 Control of cellular physiology by TM9 proteins in yeast and *Dictyostelium*. *The Journal of*
39
40 837 *Biological Chemistry* **283**, 6764-6772.
41
42
43 838 Froquet, R., le Coadic, M., Perrin, J., Cherix, N., Cornillon, S. and Cosson, P. (2012).
44
45 839 TM9/Phg1 and SadA proteins control surface expression and stability of SibA adhesion
46
47 840 molecules in *Dictyostelium*. *Molecular Biology of the Cell* **23**, 679-686.
48
49
50 841 Gomez-Valero, L., Rusniok, C., Cazalet, C. and Buchrieser, C. (2011). Comparative and
51
52 842 functional genomics of *Legionella* identified eukaryotic like proteins as key players in
53
54 843 host-pathogen interactions. *Frontiers in Microbiology* **2**, 208.
55
56
57
58
59
60

- 1
2
3 844 Grigoriev, I., Gouveia, S.M., van der Vaart, B., Demmers, J., Smyth, J.T., Honnappa, S., *et al.*
4
5 845 (2008). STIM1 is a MT-plus-end-tracking protein involved in remodeling of the ER.
6
7 846 *Current Biology* **18**, 177-182.
- 8
9
10 847 Guelly, C., Zhu, P.P., Leonardis, L., Paptic, L., Zidar, J., Schabhuttl, M., *et al.* (2011).
11
12 848 Targeted high-throughput sequencing identifies mutations in atlastin-1 as a cause of
13
14 849 hereditary sensory neuropathy type I. *American Journal of Human Genetics* **88**, 99-105.
- 15
16
17 850 Hoffmann, C., Finsel, I., Otto, A., Pfaffinger, G., Rothmeier, E., Hecker, M., *et al.* (2014).
18
19 851 Functional analysis of novel Rab GTPases identified in the proteome of purified
20
21 852 *Legionella*-containing vacuoles from macrophages. *Cellular Microbiology* **16**, 1034-1052.
- 22
23
24 853 Hu, J., Shibata, Y., Zhu, P.P., Voss, C., Rismanchi, N., Prinz, W.A., *et al.* (2009). A class of
25
26 854 dynamin-like GTPases involved in the generation of the tubular ER network. *Cell* **138**,
27
28 855 549-561.
- 29
30
31 856 Isberg, R.R., O'Connor, T.J. and Heidtman, M. (2009). The *Legionella pneumophila*
32
33 857 replication vacuole: making a cosy niche inside host cells. *Nature Reviews Microbiology* **7**,
34
35 858 13-24.
- 36
37
38 859 Journet, A., Chapel, A., Jehan, S., Adessi, C., Freeze, H., Klein, G. and Garin, J. (1999).
39
40 860 Characterization of *Dictyostelium discoideum* cathepsin D. *Journal of Cell Science* **112**,
41
42 861 3833-3843.
- 43
44
45 862 Jozsef, L., Tashiro, K., Kuo, A., Park, E.J., Skoura, A., Albinsson, S., *et al.* (2014). Reticulon
46
47 863 4 is necessary for endoplasmic reticulum tubulation, STIM1-Orai1 coupling, and store-
48
49 864 operated calcium entry. *The Journal of Biological Chemistry* **289**, 9380-9395.
- 50
51
52 865 Kagan, J.C. and Roy, C.R. (2002). *Legionella* phagosomes intercept vesicular traffic from
53
54 866 endoplasmic reticulum exit sites. *Nature Cell Biology* **4**, 945-954.
- 55
56
57
58
59
60

- 1
2
3 867 Kagan, J.C., Stein, M.P., Pypaert, M. and Roy, C.R. (2004). *Legionella* subvert the functions
4
5 868 of Rab1 and Sec22b to create a replicative organelle. *The Journal of Experimental*
6
7 869 *Medicine* **199**, 1201-1211.
- 8
9
10 870 Kim, K.T., Moon, Y., Jang, Y., Lee, K.T., Lee, C., Jun, Y. and Lee, S. (2017). Molecular
11
12 871 mechanisms of atlastin-mediated ER membrane fusion revealed by a FRET-based single-
13
14 872 vesicle fusion assay. *Scientific Reports* **7**, 8700.
- 15
16
17 873 Klemm, R.W., Norton, J.P., Cole, R.A., Li, C.S., Park, S.H., Crane, M.M., *et al.* (2013). A
18
19 874 conserved role for atlastin GTPases in regulating lipid droplet size. *Cell Reports* **3**, 1465-
20
21 875 1475.
- 22
23
24 876 Klopfenstein, D.R., Kappeler, F. and Hauri, H.P. (1998). A novel direct interaction of
25
26 877 endoplasmic reticulum with microtubules. *The EMBO Journal* **17**, 6168-6177.
- 27
28 878 Krols, M., Detry, S., Asselbergh, B., Almeida-Souza, L., Kremer, A., Lippens, S., *et al.*
29
30 879 (2018). Sensory-neuropathy-causing mutations in ATL3 cause aberrant ER membrane
31
32 880 tethering. *Cell Reports* **23**, 2026-2038.
- 33
34
35 881 Lai, Y.S., Stefano, G. and Brandizzi, F. (2014). ER stress signaling requires RHD3, a
36
37 882 functionally conserved ER-shaping GTPase. *Journal of Cell Science* **127**, 3227-3232.
- 38
39
40 883 Lamrabet, O., Jauslin, T., Lima, W.C., Leippe, M. and Cosson, P. (2020). The multifarious
41
42 884 lysozyme arsenal of *Dictyostelium discoideum*. *Developmental and Comparative*
43
44 885 *Immunology* **107**, 103645.
- 45
46
47 886 Le Coadic, M., Froquet, R., Lima, W.C., Dias, M., Marchetti, A. and Cosson, P. (2013).
48
49 887 Phg1/TM9 proteins control intracellular killing of bacteria by determining cellular levels of
50
51 888 the Kill1 sulfotransferase in *Dictyostelium*. *PloS One* **8**, e53259.
- 52
53
54 889 Lee, M., Paik, S.K., Lee, M.J., Kim, Y.J., Kim, S., Nahm, M., *et al.* (2009). *Drosophila*
55
56 890 atlastin regulates the stability of muscle microtubules and is required for synapse
57
58 891 development. *Developmental Biology* **330**, 250-262.
- 59
60

- 1
2
3 892 Liang, J.R., Lingeman, E., Ahmed, S. and Corn, J.E. (2018). Atlastins remodel the
4
5 893 endoplasmic reticulum for selective autophagy. *The Journal of Cell Biology* **217**, 3354-
6
7 894 3367.
- 8
9
10 895 Lima, W.C., Leuba, F., Soldati, T. and Cosson, P. (2012). Mucolipin controls lysosome
11
12 896 exocytosis in *Dictyostelium*. *Journal of Cell Science* **125**, 2315-2322.
- 13
14 897 Liu, T.Y., Bian, X., Romano, F.B., Shemesh, T., Rapoport, T.A. and Hu, J. (2015). Cis and
15
16 898 trans interactions between atlastin molecules during membrane fusion. *Proceedings of the*
17
18 899 *National Academy of Sciences of the United States of America* **112**, E1851-1860.
- 20
21 900 Liu, T.Y., Bian, X., Sun, S., Hu, X., Klemm, R.W., Prinz, W.A., *et al.* (2012). Lipid
22
23 901 interaction of the C terminus and association of the transmembrane segments facilitate
24
25 902 atlastin-mediated homotypic endoplasmic reticulum fusion. *Proceedings of the National*
26
27 903 *Academy of Sciences of the United States of America* **109**, E2146-2154.
- 28
29 904 Malchow, D., Nagele, B., Schwarz, H. and Gerisch, G. (1972). Membrane-bound cyclic AMP
30
31 905 phosphodiesterase in chemotactically responding cells of *Dictyostelium discoideum*.
32
33 906 *European Journal of Biochemistry / FEBS* **28**, 136-142.
- 34
35 907 Niu, L., Ma, T., Yang, F., Yan, B., Tang, X., Yin, H., *et al.* (2019). Atlastin-mediated
36
37 908 membrane tethering is critical for cargo mobility and exit from the endoplasmic reticulum.
38
39 909 *Proceedings of the National Academy of Sciences of the United States of America* **116**,
40
41 910 14029-14038.
- 42
43 911 O'Donnell, J.P., Byrnes, L.J., Cooley, R.B. and Sonderrmann, H. (2018). A hereditary spastic
44
45 912 paraplegia-associated atlastin variant exhibits defective allosteric coupling in the catalytic
46
47 913 core. *The Journal of Biological Chemistry* **293**, 687-700.
- 48
49 914 Ogawa-Goto, K., Tanaka, K., Ueno, T., Tanaka, K., Kurata, T., Sata, T. and Irie, S. (2007).
50
51 915 p180 is involved in the interaction between the endoplasmic reticulum and microtubules
52
53
54
55
56
57
58
59
60

- 1
2
3 916 through a novel microtubule-binding and bundling domain. *Molecular Biology of the Cell*
4
5 917 **18**, 3741-3751.
6
7
8 918 Orso, G., Pendin, D., Liu, S., Tosetto, J., Moss, T.J., Faust, J.E., *et al.* (2009). Homotypic
9
10 919 fusion of ER membranes requires the dynamin-like GTPase atlastin. *Nature* **460**, 978-983.
11
12 920 Park, S.H., Zhu, P.P., Parker, R.L. and Blackstone, C. (2010). Hereditary spastic paraplegia
13
14 921 proteins REEP1, spastin, and atlastin-1 coordinate microtubule interactions with the
15
16 922 tubular ER network. *The Journal of Clinical Investigation* **120**, 1097-1110.
17
18
19 923 Pawar, S., Ungricht, R., Tiefenboeck, P., Leroux, J.C. and Kutay, U. (2017). Efficient protein
20
21 924 targeting to the inner nuclear membrane requires atlastin-dependent maintenance of ER
22
23 925 topology. *eLife* **6**, e28202.
24
25
26 926 Personnic, N., Bärlocher, K., Finsel, I. and Hilbi, H. (2016). Subversion of retrograde
27
28 927 trafficking by translocated pathogen effectors. *Trends in Microbiology* **24**, 450-462.
29
30
31 928 Phillips, M.J. and Voeltz, G.K. (2016). Structure and function of ER membrane contact sites
32
33 929 with other organelles. *Nature Reviews Molecular and Cell Biology* **17**, 69-82.
34
35
36 930 Rismanchi, N., Soderblom, C., Stadler, J., Zhu, P.P. and Blackstone, C. (2008). Atlastin
37
38 931 GTPases are required for Golgi apparatus and ER morphogenesis. *Human molecular*
39
40 932 *genetics* **17**, 1591-1604.
41
42
43 933 Robinson, C.G. and Roy, C.R. (2006). Attachment and fusion of endoplasmic reticulum with
44
45 934 vacuoles containing *Legionella pneumophila*. *Cellular Microbiology* **8**, 793-805.
46
47
48 935 Rogers, J.V., McMahon, C., Baryshnikova, A., Hughson, F.M. and Rose, M.D. (2014). ER-
49
50 936 associated retrograde SNAREs and the Dsl1 complex mediate an alternative, Sey1p-
51
52 937 independent homotypic ER fusion pathway. *Molecular Biology of the Cell* **25**, 3401-3412.
53
54
55 938 Rothmeier, E., Pfaffinger, G., Hoffmann, C., Harrison, C.F., Grabmayr, H., Repnik, U., *et al.*
56
57 939 (2013). Activation of Ran GTPase by a *Legionella* effector promotes microtubule
58
59 940 polymerization, pathogen vacuole motility and infection. *PLoS Pathogens* **9**, e1003598.
60

- 1
2
3 941 Salinas, S., Proukakis, C., Crosby, A. and Warner, T.T. (2008). Hereditary spastic paraplegia:
4
5 942 clinical features and pathogenetic mechanisms. *Lancet Neurology* **7**, 1127-1138.
6
7
8 943 Sanderson, C.M., Connell, J.W., Edwards, T.L., Bright, N.A., Duley, S., Thompson, A., *et al.*
9
10 944 (2006). Spastin and atlastin, two proteins mutated in autosomal-dominant hereditary
11
12 945 spastic paraplegia, are binding partners. *Human molecular genetics* **15**, 307-318.
13
14
15 946 Schwarz, D.S. and Blower, M.D. (2016). The endoplasmic reticulum: structure, function and
16
17 947 response to cellular signaling. *Cellular and Molecular Life Sciences* **73**, 79-94.
18
19
20 948 Sherwood, R.K. and Roy, C.R. (2016). Autophagy evasion and endoplasmic reticulum
21
22 949 subversion: the Yin and Yang of *Legionella* intracellular infection. *Annual Reviews in*
23
24 950 *Microbiology* **70**, 413-433.
25
26
27 951 Shibata, Y., Hu, J., Kozlov, M.M. and Rapoport, T.A. (2009). Mechanisms shaping the
28
29 952 membranes of cellular organelles. *Annual Reviews of Cell and Developmental Biology* **25**,
30
31 953 329-354.
32
33
34 954 Shibata, Y., Voeltz, G.K. and Rapoport, T.A. (2006). Rough sheets and smooth tubules. *Cell*
35
36 955 **126**, 435-439.
37
38
39 956 Smith, M. and Wilkinson, S. (2017). ER homeostasis and autophagy. *Essays in Biochemistry*
40
41 957 **61**, 625-635.
42
43
44 958 Solomon, J.M. and Isberg, R.R. (2000). Growth of *Legionella pneumophila* in *Dictyostelium*
45
46 959 *discoideum*: a novel system for genetic analysis of host-pathogen interactions. *Trends in*
47
48 960 *Microbiology* **8**, 478-480.
49
50
51 961 Song, S., Tan, J., Miao, Y. and Zhang, Q. (2018). Crosstalk of ER stress-mediated autophagy
52
53 962 and ER-phagy: Involvement of UPR and the core autophagy machinery. *Journal of Cell*
54
55 963 *Physiology* **233**, 3867-3874.
56
57
58 964 Stefano, G., Renna, L. and Brandizzi, F. (2014). The endoplasmic reticulum exerts control
59
60 965 over organelle streaming during cell expansion. *Journal of Cell Science* **127**, 947-953.

- 1
2
3 966 Stefano, G., Renna, L., Lai, Y., Slabaugh, E., Mannino, N., Buono, R.A., *et al.* (2015). ER
4
5 967 network homeostasis is critical for plant endosome streaming and endocytosis. *Cell*
6
7 968 *Discovery* **1**, 15033.
- 9
10 969 Steiner, B., Swart, A.L., Welin, A., Weber, S., Personnic, N., Kaech, A., *et al.* (2017). ER
11
12 970 remodeling by the large GTPase atlastin promotes vacuolar growth of *Legionella*
13
14 971 *pneumophila*. *EMBO Reports* **18**, 1817-1836.
- 16
17 972 Steiner, B., Weber, S. and Hilbi, H. (2018a). Formation of the *Legionella*-containing vacuole:
18
19 973 phosphoinositide conversion, GTPase modulation and ER dynamics. *International Journal*
20
21 974 *of Medical Microbiology* **308**, 49-57.
- 23
24 975 Steiner, B., Weber, S., Kaech, A., Ziegler, U. and Hilbi, H. (2018b). The large GTPase
25
26 976 atlastin controls ER remodeling around a pathogen vacuole. *Communicative & Integrative*
27
28 977 *Biology* **11**, 1-5.
- 30
31 978 Stolz, A. and Grumati, P. (2019). The various shades of ER-phagy. *The FEBS Journal* **286**,
32
33 979 4642-4649.
- 35
36 980 Swanson, M.S. and Isberg, R.R. (1995). Association of *Legionella pneumophila* with the
37
38 981 macrophage endoplasmic reticulum. *Infection and Immunity* **63**, 3609-3620.
- 40
41 982 Swart, A.L., Harrison, C.F., Eichinger, L., Steinert, M. and Hilbi, H. (2018). *Acanthamoeba*
42
43 983 and *Dictyostelium* as cellular models for *Legionella* infection. *Frontiers in Cellular and*
44
45 984 *Infection Microbiology* **8**, 61.
- 46
47 985 Swart, A.L. and Hilbi, H. (2020a). Phosphoinositides and the fate of *Legionella* in
48
49 986 phagocytes. *Frontiers in Immunology* **11**, 25.
- 51
52 987 Swart, A.L., Steiner, B., Gomez-Valero, L., Schutz, S., Hannemann, M., Janning, P., *et al.*
53
54 988 (2020b). Divergent evolution of *Legionella* RCC1 repeat effectors defines the range of Ran
55
56 989 GTPase cycle targets. *mBio* **11**, e00405-20.
- 57
58
59
60

- 1
2
3 990 Voeltz, G.K., Prinz, W.A., Shibata, Y., Rist, J.M. and Rapoport, T.A. (2006). A class of
4
5 991 membrane proteins shaping the tubular endoplasmic reticulum. *Cell* **124**, 573-586.
6
7
8 992 Voss, C., Lahiri, S., Young, B.P., Loewen, C.J. and Prinz, W.A. (2012). ER-shaping proteins
9
10 993 facilitate lipid exchange between the ER and mitochondria in *S. cerevisiae*. *Journal of Cell*
11
12 994 *Science* **125**, 4791-4799.
13
14
15 995 Wang, S., Tukachinsky, H., Romano, F.B. and Rapoport, T.A. (2016). Cooperation of the ER-
16
17 996 shaping proteins atlastin, lunapark, and reticulons to generate a tubular membrane network.
18
19 997 *eLife* **5**, e18605.
20
21
22 998 Weber, S. and Hilbi, H. (2014a). Live cell imaging of phosphoinositide dynamics during
23
24 999 *Legionella* infection. *Methods in Molecular Biology* **1197**, 153-167.
25
26 1000 Weber, S., Steiner, B., Welin, A. and Hilbi, H. (2018). *Legionella*-containing vacuoles
27
28 1001 capture PtdIns(4)P-rich vesicles derived from the Golgi apparatus. *mBio* **9**, e02420-18.
29
30
31 1002 Weber, S., Wagner, M. and Hilbi, H. (2014b). Live-cell imaging of phosphoinositide
32
33 1003 dynamics and membrane architecture during *Legionella* infection. *mBio* **5**, e00839-13.
34
35 1004 Welin, A., Weber, S. and Hilbi, H. (2018). Quantitative imaging flow cytometry of
36
37 1005 *Legionella*-infected *Dictyostelium* amoebae reveals the impact of retrograde trafficking on
38
39 1006 pathogen vacuole composition. *Applied and Environmental Microbiology* **84**, e00158-18.
40
41
42 1007 Wilkinson, S. (2019). ER-phagy: shaping up and destressing the endoplasmic reticulum. *The*
43
44 1008 *FEBS Journal* **286**, 2645-2663.
45
46
47 1009 Wilkinson, S. (2020). Emerging principles of selective ER autophagy. *Journal of Molecular*
48
49 1010 *Biology* **432**, 185-205.
50
51
52 1011 Zhang, D., Vjestica, A. and Oliferenko, S. (2010). The cortical ER network limits the
53
54 1012 permissive zone for actomyosin ring assembly. *Current Biology* **20**, 1029-1034.
55
56 1013 Zhang, M., Wu, F., Shi, J., Zhu, Y., Zhu, Z., Gong, Q. and Hu, J. (2013). ROOT HAIR
57
58 1014 DEFECTIVE3 family of dynamin-like GTPases mediates homotypic endoplasmic
59
60

- 1
2
3 1015 reticulum fusion and is essential for *Arabidopsis* development. *Plant Physiology* **163**, 713-
4
5 1016 720.
6
7 1017 Zhao, G., Zhu, P.P., Renvoise, B., Maldonado-Baez, L., Park, S.H. and Blackstone, C. (2016).
8 1018 Mammalian knock out cells reveal prominent roles for atlastin GTPases in ER network
9
10 1019 morphology. *Experimental Cell Research* **349**, 32-44.
11
12 1020 Zhu, Y., Zhang, G., Lin, S., Shi, J., Zhang, H. and Hu, J. (2018). Sec61beta facilitates the
13
14 1021 maintenance of endoplasmic reticulum homeostasis by associating microtubules. *Protein*
15
16 1022 & *Cell* **9**, 616-628.
17
18
19
20
21
22
23
24 1024
25
26
27
28
29
30
31
32
33
34
35
36
37
38
39
40
41
42
43
44
45
46
47
48
49
50
51
52
53
54
55
56
57
58
59
60

For Peer Review

1025 **FIGURE LEGENDS**

1026 **FIGURE 1** Genomic deletion of *D. discoideum sey1* and basic mutant characterization.

1027 **(a)** Schematic representation of the strategy used to inactivate the *D. discoideum sey1* gene by
1028 insertion of the blasticidin resistance-encoding gene (BsR) by double recombination. *Sey1*
1029 comprises a large guanosine triphosphatase (GTPase) domain followed by a three-helix
1030 bundle (3HB) and two adjacent transmembrane motifs (TMs). In $\Delta sey1$ cells, the protein
1031 sequence from amino acid residues P149 to K588 is deleted. **(b)** Phase contrast microscopy
1032 and **(c)** histogram of cell-contact area of live cells on tissue culture dishes determined after
1033 binarization of images (ImageJ) (n=100) revealed that $\Delta sey1$ cells are enlarged compared to
1034 parental cells (Ax3). Scale bar, 10 μm . **(d)** Representative distribution of cell diameters
1035 measured by electric current exclusion (CASY technology). Compared to Ax3 cells, $\Delta sey1$
1036 cells show a greater diameter heterogeneity with a mean diameter of $10.24 \pm 0.15 \mu\text{m}$ instead
1037 of $9.51 \pm 0.24 \mu\text{m}$ in Ax3 cells (data represent the average and s.e.m. of four independent
1038 experiments) **(e)** Histogram showing the distribution of nuclei/cell for the indicated *D.*
1039 *discoideum* strains (Ax3, $\Delta sey1$). Cells were stained with DAPI (4',6-diamidino-2-
1040 phenylindole; blue). 32.7% of $\Delta sey1$ cells showed two or more nuclei in contrast to 10.2% for
1041 Ax3 cells (n=100 cells). **(f)** Growth curves of *D. discoideum* strains cultivated in Petri-dishes
1042 plotted as a function of time (in hours, h). Compared to Ax3 cells, $\Delta sey1$ cells show a reduced
1043 growth rate. Doubling times are indicated (data represent the average and s.e.m. of three
1044 independent experiments). **(g)** Aggregation and development of Ax3 and $\Delta sey1$ cells plated
1045 on solid starvation plates and incubated at 22°C. Cellular aggregates were observed after 6 h
1046 and fruiting bodies after 24 h for both cell lines. Scale bar, 0.5 mm

1048 **FIGURE 2** *D. discoideum* $\Delta sey1$ shows aberrant ER morphology and dynamics.

1
2
3 1049 (a) ER morphology in Ax3 and $\Delta sey1$ cells analyzed by confocal microscopy after
4
5 1050 immunolabeling of the ER-resident enzyme protein disulfide isomerase (PDI). Compared to
6
7
8 1051 the Ax3 parental strain, $\Delta sey1$ cells showed clumps of PDI-positive membranous structures at
9
10 1052 the cell periphery and a few interconnected ER tubules (red arrowheads). Nuclei were stained
11
12 1053 with DAPI (in blue). Scale bars, 5 μm . (b) Representative confocal fluorescence micrographs
13
14 1054 of dually labeled *D. discoideum* Ax3 or $\Delta sey1$ mutant cells producing the ER marker calnexin
15
16 1055 A-GFP (CnxA-GFP) and the PtdIns(4)*P*-binding probe P4C-mCherry. Arrowheads, clumped
17
18 1056 peripheral ER. Scale bars, 3 μm . (c) Snapshots of time-lapse video microscopy analysis of
19
20 1057 amoebae producing calnexin A-GFP. The ER nodular clumps observed in $\Delta sey1$ cells appear
21
22 1058 mostly static (white arrowheads) in contrast to the vivid dynamics of ER tubules in mutant
23
24 1059 and parental *D. discoideum* strains (red arrowheads). N, nucleus. Scale bars, 5 μm . (d)
25
26 1060 Electron micrographs of Ax3 and $\Delta sey1$ cells. N, nucleus; arrowheads, rough ER. Scale bars,
27
28 1061 1 μm .

29
30
31
32
33
34 1062
35
36 1063 **FIGURE 3** Analysis of endocytic functions and growth on bacteria of $\Delta sey1$ cells.

37
38 1064 (a) Fluid-phase uptake of dextran coupled to Alexa-Fluor-647 was measured by flow
39
40 1065 cytometry and expressed as the percentage of the maximal uptake in Ax3 cells. (b) Exocytosis
41
42 1066 was analyzed in cells preincubated for 4 h with Alexa-Fluor-647-dextran to fully load all
43
44 1067 endocytic compartments. After incubation in dextran-free medium for different periods of
45
46 1068 time, retained intracellular fluorescence was measured by flow cytometry and expressed as
47
48 1069 the percentage of the initial fluorescence. (c) Representative images of the growth of cells on
49
50 1070 lawns of *K. pneumoniae* observed after 5 days ($n > 3$). $\Delta sey1$ cells were unable to grow on
51
52 1071 these bacterial lawns, whereas the production of GFP-Sey1 partially complemented this
53
54 1072 defect. (d) Schematic representation of cell capacities to grow on different bacterial lawns.
55
56 1073 $\Delta sey1$ cells showed total growth inhibition on lawns of Gram-negative *K. pneumoniae* (*K.*

1
2
3 1074 *pneum.*) and *E. coli* B/r and severely reduced growth rates on lawns of Gram-positive *B.*
4
5 1075 *subtilis* and *M. luteus*. Cell growth on several bacterial species was assessed as shown in (c) in
6
7
8 1076 three independent experiments and scored from 4 (efficient growth in all tested cell numbers)
9
10 1077 to 0 (no growth). Colored squares indicate the average score (green 4, yellow 3, orange 2, and
11
12 1078 red 0-1). (e) Uptake of *K. pneumoniae* was measured by flow cytometry after incubation of
13
14 1079 cells with GFP-producing bacteria for 20 min. Results are expressed as the percentage of
15
16
17 1080 uptake in Ax3 cells. (f) Phagocytic rates of Ax3 and Δ *sey1* cells incubated with fluorescent
18
19 1081 beads. Cells were incubated with 1 μ m YG-labeled beads, and at the indicated time points, the
20
21
22 1082 internal fluorescence was measured by flow cytometry and expressed as the percent of
23
24 1083 maximal uptake by Ax3 cells. (g) Killing of internalized bacteria was measured upon
25
26 1084 incubation of Ax3 or Δ *sey1* cells with *K. pneumoniae*. At the indicated time points, samples
27
28
29 1085 were treated with Triton X-100 to selectively lyse amoebae and plated on LB-agar plates.
30
31 1086 Bacterial clones were counted after overnight incubation at 37°C. Data are expressed as the
32
33 1087 percent of surviving bacteria. All data in this figure are normalized to protein content in cells
34
35 1088 and represent the mean and s.e.m. of three independent experiments (not significant, ns: $P >$
36
37
38 1089 0.05, $**P < 0.01$).

1090

1091 **FIGURE 4** Hypersecretion of lysosomal enzymes by Δ *sey1* cells.

1092 (a) The enzymatic activity of lysozymes in cell lysates was measured by the reduction of
1093 turbidity of heat-killed *Micrococcus lysodeikticus* in suspension. Results are expressed as the
1094 percentage of activity of strain Ax3 (left panel). When bacteria are included in agarose gels,
1095 halos around diluted cell lysate deposits form proportionally to the extent of bacterial lysis
1096 (right panel) providing a visual estimate of enzymatic activities. (b) α -mannosidase and
1097 cathepsin D (CtsD) enzymatic activities were measured in cellular pellets (internal pool) and
1098 extracellular medium (secreted pool) after incubation of the Ax3 and Δ *sey1* strains indicated

1
2
3 1099 in culture medium for 24 h. Results are expressed as the percentage of secreted activities
4
5 1100 relatively to total internal and secreted activities. (c) Cathepsin D production by the Ax3 and
6
7 1101 $\Delta sey1$ strains indicated. Representative samples of cathepsin D (CtsD, 44 kDa) protein
8
9 1102 quantity determined by Western blot of whole cell lysates with an anti-CtsD antibody.
10
11 1103 Immunoblotting with an anti-PDI antibody was carried out to control protein amounts of
12
13 1104 loaded material. (d) Histogram showing calculated ratio between CtsD and PDI signals in
14
15 1105 Western blots quantified using the Image lab analysis software. Results are normalized to the
16
17 1106 CtsD/PDI ratio in Ax3 cells. (e) Intracellular proteolysis was measured by feeding cells with
18
19 1107 DQ Green-BSA coated beads and measuring unquenching of the fluorophore after incubation
20
21 1108 for 1 h. Proteolysis in $\Delta sey1$ cells is expressed as the percentage of Ax3 activity. All data
22
23 1109 presented in this figure are the mean and s.e.m. of three independent experiments (not
24
25 1110 significant, ns: $P > 0.05$, $*P < 0.05$, $**P < 0.01$, $****P < 0.0001$).

30
31 1111

32
33 1112 **FIGURE 5** *D. discoideum* $\Delta sey1$ is impaired for cell motility.

34
35 1113 (a) Time-lapse video confocal microscopy of cell motility using single cell tracking analysis.
36
37 1114 The indicated Ax3 or $\Delta sey1$ strains were incubated in HL5 medium and imaged by spinning
38
39 1115 disk confocal microscopy. Randomly moving cells were imaged every 30 s for 30 min. Tracks
40
41 1116 of 15 randomly sampled cells are shown centered at the origin. The motility defect of $\Delta sey1$
42
43 1117 cells was restored upon ectopic production of GFP-Sey1 but not of the catalytically inactive
44
45 1118 Sey1_K154A mutant. (b) Quantification of the maximum distance from the origin of
46
47 1119 individual cells of each cell line. The median is indicated by a line in each box extending from
48
49 1120 the upper and lower quartiles (not significant, ns: $P > 0.05$, $***P < 0.001$).

50
51 1121

52
53 1122 **FIGURE 6** Analysis of the UPR pathway in *D. discoideum* $\Delta sey1$.

1
2
3 1123 (a) Histogram of cell viability after addition of 1.5 $\mu\text{g}/\text{mL}$ tunicamycin (TN) for the indicated
4
5 1124 period of times. Viability was measured by flow cytometry analysis as exclusion of propidium
6
7 1125 iodide. Results are the mean and s.e.m. of three independent experiments (not significant, ns:
8
9 1126 $P > 0.05$, $**P < 0.01$, $***P < 0.001$). (b) The indicated cell lines were incubated with 1.5
10
11 1127 $\mu\text{g}/\text{mL}$ tunicamycin (TN) and observed by phase contrast microscopy after 48 h of incubation.
12
13 1128 Dead cells are indicated by red arrows. Scale bars, 10 μm . (c) Effect of the TN concentration
14
15 1129 on cell viability after 48 h of incubation. Cell viability was determined as above. (d)
16
17 1130 Representative Western blot analysis of CdcD and PDI protein production in cells after
18
19 1131 addition of 1.5 $\mu\text{g}/\text{mL}$ TN for 24 h. (e) Quantification of signals in Western blots for CdcD
20
21 1132 and PDI bands. Data correspond to the quotient of CdcD or PDI divided by EHD signals and
22
23 1133 normalized to corresponding signals in Ax3. Results are the mean and s.e.m. of three and five
24
25 1134 independent experiments for CdcD and PDI, respectively (not significant, ns: $P > 0.05$, $*P <$
26
27 1135 0.05 , $**P < 0.01$, $****P < 0.0001$).

1136

1137 **FIGURE 7** *D. discoideum* Δsey1 is defective for intracellular replication of *L. pneumophila*
1138 and rough ER recruitment.

1139 (a) *D. discoideum* Ax3 or Δsey1 producing GFP (pDM317) were infected (MOI 1) with
1140 (filled symbols) mCherry-producing *L. pneumophila* JR32 or (empty symbols) ΔicmT
1141 (pNP102) for 6 days. Intracellular replication of the bacteria was assessed by colony-forming
1142 units (CFU), of which the number of CFU per mL was calculated and plotted. Data represent
1143 mean \pm SD of two independent experiments in technical triplicates ($***P < 0.001$). (b) *D.*
1144 *discoideum* Ax3 or Δsey1 producing GFP (pDM317) were infected (MOI 50) with mCherry-
1145 producing *L. pneumophila* ΔicmT (pNP102) for the time indicated. Percentage of surviving
1146 bacteria was derived from CFU. Data represent mean \pm SD of two independent experiments
1147 in technical triplicates (not significant, ns: $P > 0.05$). (c) *D. discoideum* Ax3 or Δsey1

1
2
3 1148 producing GFP (pDM317) or $\Delta sey1$ expressing GFP-Sey1 (pBS001) were infected (MOI 10)
4
5 1149 for 2 h or 8 h with mCherry-producing *L. pneumophila* JR32 (upper panels) or $\Delta icmT$ (lower
6
7 1150 panels). Samples were fixed, stained with uranyl acetate, embedded in Epon/Araldite and
8
9 1151 analyzed by electron microscopy. Star: *L. pneumophila*; arrowhead: rough endoplasmic
10
11 1152 reticulum (ER). Scale bars, 500 nm.
12
13
14
15 1153

16
17 1154 **FIGURE 8** *D. discoideum* $\Delta sey1$ cells are impaired for LCV expansion.

18
19 1155 (a) Representative confocal fluorescence micrographs of dually labeled *D. discoideum* Ax3
20
21 1156 (upper panel) or $\Delta sey1$ mutant (lower panel) producing calnexin-GFP (CnxA-GFP) and P4C-
22
23 1157 mCherry, infected (MOI 5, 2 h) with mCerulean-producing *L. pneumophila* JR32 (pNP99).
24
25 1158 Scale bars, 3 μm . (b) Imaging flow cytometry (IFC) analysis of dually labelled *D. discoideum*
26
27 1159 Ax3 and $\Delta sey1$ mutant producing calnexin-GFP (CnxA-GFP) and P4C-mCherry, infected
28
29 1160 (MOI 5) with mPlum-producing *L. pneumophila* JR32 (pAW014). Representative images at 6
30
31 1161 h p.i. are depicted; scale bars, 7 μm (top panel). Quantification of CnxA-GFP or P4C-
32
33 1162 mCherry localizing to LCVs during early time points of infection (bottom panel). Number of
34
35 1163 events per sample, n = 111-1565. Data represent mean \pm SD of three independent experiments
36
37 1164 (* $P < 0.05$, *** $P < 0.001$). (c) Representative confocal fluorescence micrographs of dually
38
39 1165 labeled *D. discoideum* Ax3 (upper panels) or $\Delta sey1$ mutant (lower panels) producing CnxA-
40
41 1166 GFP and P4C-mCherry, infected (MOI 5) with mCerulean-producing *L. pneumophila* JR32
42
43 1167 (pNP99) for 2 h, 8 h, 16 h or 24 h. Scale bars, 3 μm . (d) Quantification of (C) LCV area at the
44
45 1168 analyzed time points (n = 100). Data represent mean \pm 95% CI of three independent
46
47 1169 experiments (*** $P < 0.001$).
48
49
50
51
52
53
54 1170
55
56
57
58
59
60

1
2
3 1171 SUPPORTING INFORMATION
4

5
6 1172 **FIGURE S1** Confocal microscopy analysis of the ER morphology upon ectopic production
7
8 1173 of GFP-Sey1, GFP-Sey1_K154A or GFP-Rtnlc.
9

10 1174

11
12 1175 **FIGURE S2** Confocal microscopy analysis of Sec22b, Ufe1 and Use1 localization.
13
14

15 1176

16
17 1177 **FIGURE S3** Confocal microscopy analysis of intracellular compartments and microtubule
18
19 1178 architecture.
20

21 1179

22
23
24 1180 **FIGURE S4** Confocal microscopy analysis of PtdIns(3)*P* and PtdIns(4)*P* localization and
25
26 1181 actin protrusions.
27

28 1182

29
30
31 1183 **FIGURE S5** Analysis of lysosomal enzyme secretion, carbohydrate processing and
32
33 1184 acidification of endocytic compartments.
34

35 1185

36
37
38 1186 **FIGURE S6** *D. discoideum* Δ *sey1* cells are defective for intracellular replication of *L.*
39
40 1187 *pneumophila* and LCV expansion.
41

42 1188

43
44
45 1189 **FIGURE S7** Schematic representation of the strategies followed for genetic inactivation of
46
47 1190 *sey1* or *rtnlc*, and PCR-based validation.
48

49 1191

50
51 1192 **TABLE S1** Strains and plasmids used in this study.
52

53 1193

54
55
56 1194 **TABLE S2** Oligonucleotides used in this study.
57

58 1195

1
2
3 1196 **TABLE S3** Antibodies used in this study.
4

5 1197
6

7
8 1198 **MOVIE S1** Time-lapse video microscopy analysis of Ax3 cells producing the ER marker,
9

10 1199 GFP-calnexin. Images were taken every second for 2 min.
11

12 1200
13

14
15 1201 **MOVIE S2** Time-lapse video microscopy analysis of $\Delta sey1$ cells producing the ER marker,
16

17 1202 GFP-calnexin. Images were taken every second for 2 min.
18

19 1203
20

21
22 1204 **MOVIE S3** Time-lapse video microscopy analysis of Ax3 cells producing the cytoskeleton
23

24 1205 protein tubulin A, GFP-TubA. Images were taken every second for 2 min.
25

26 1206
27

28
29 1207 **MOVIE S4** Time-lapse video microscopy analysis of $\Delta sey1$ cells producing the cytoskeleton
30

31 1208 protein tubulin A, GFP-TubA. Images were taken every second for 2 min.
32

33 1209
34
35
36
37
38
39
40
41
42
43
44
45
46
47
48
49
50
51
52
53
54
55
56
57
58
59
60

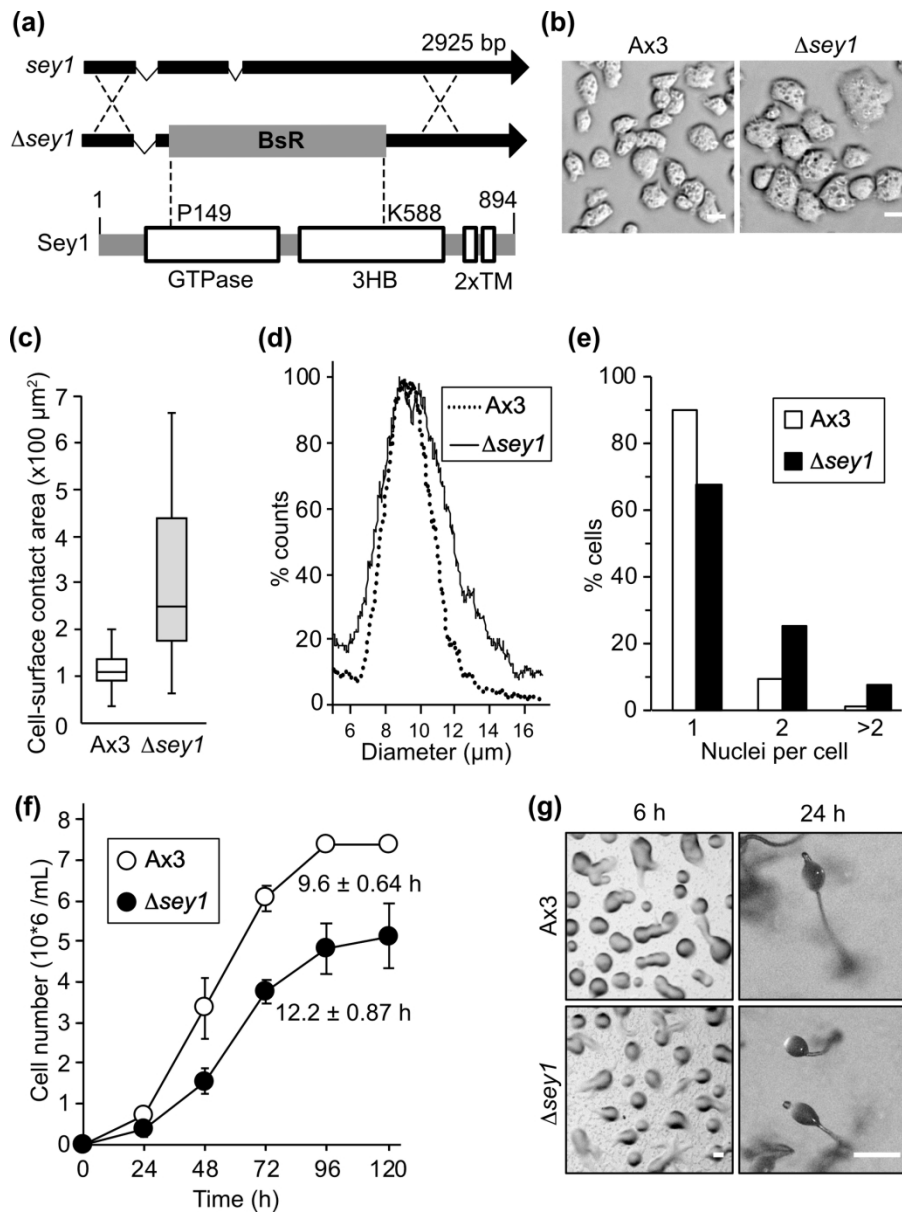


Figure 1

162x215mm (300 x 300 DPI)

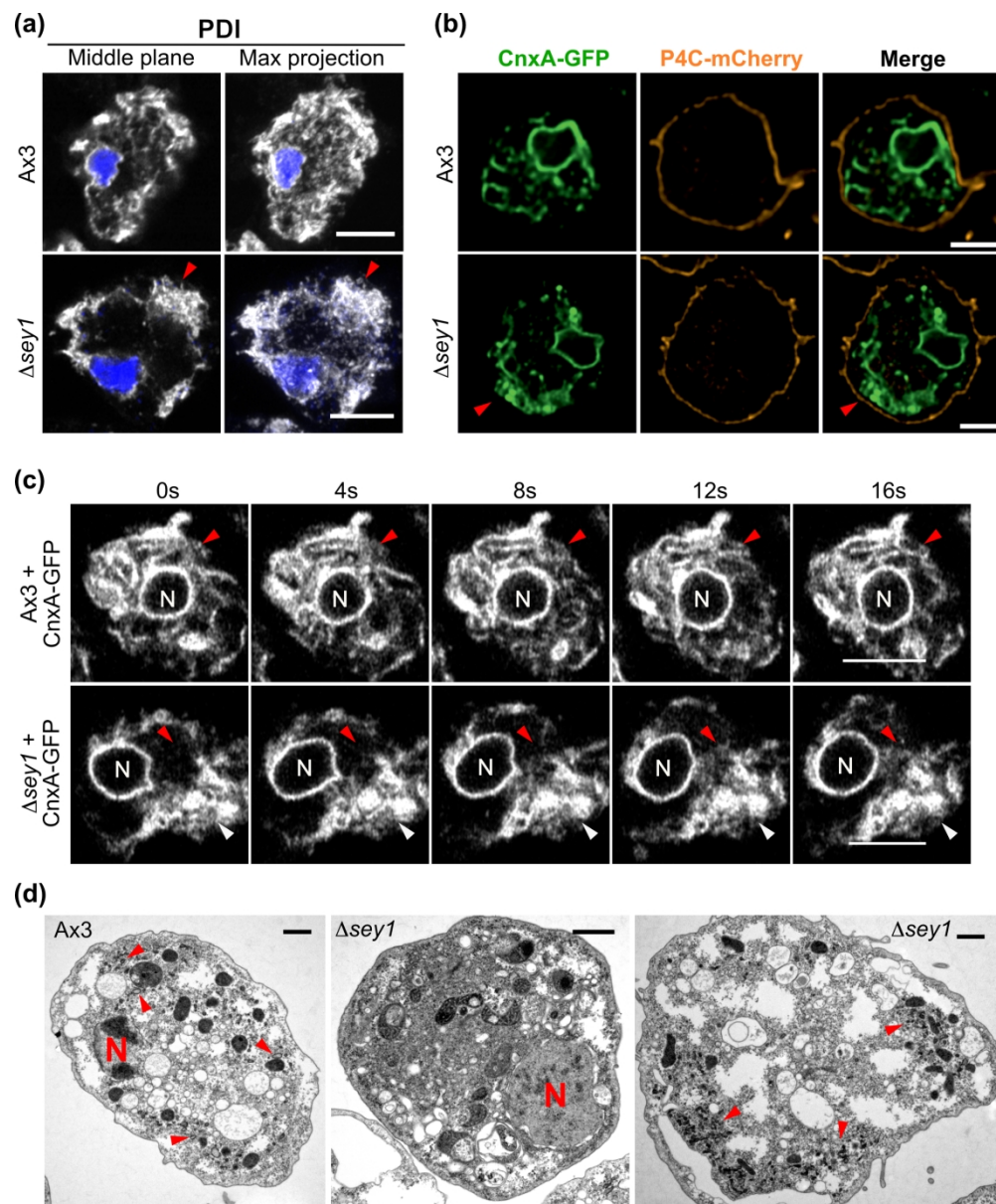


Figure 2

186x225mm (300 x 300 DPI)

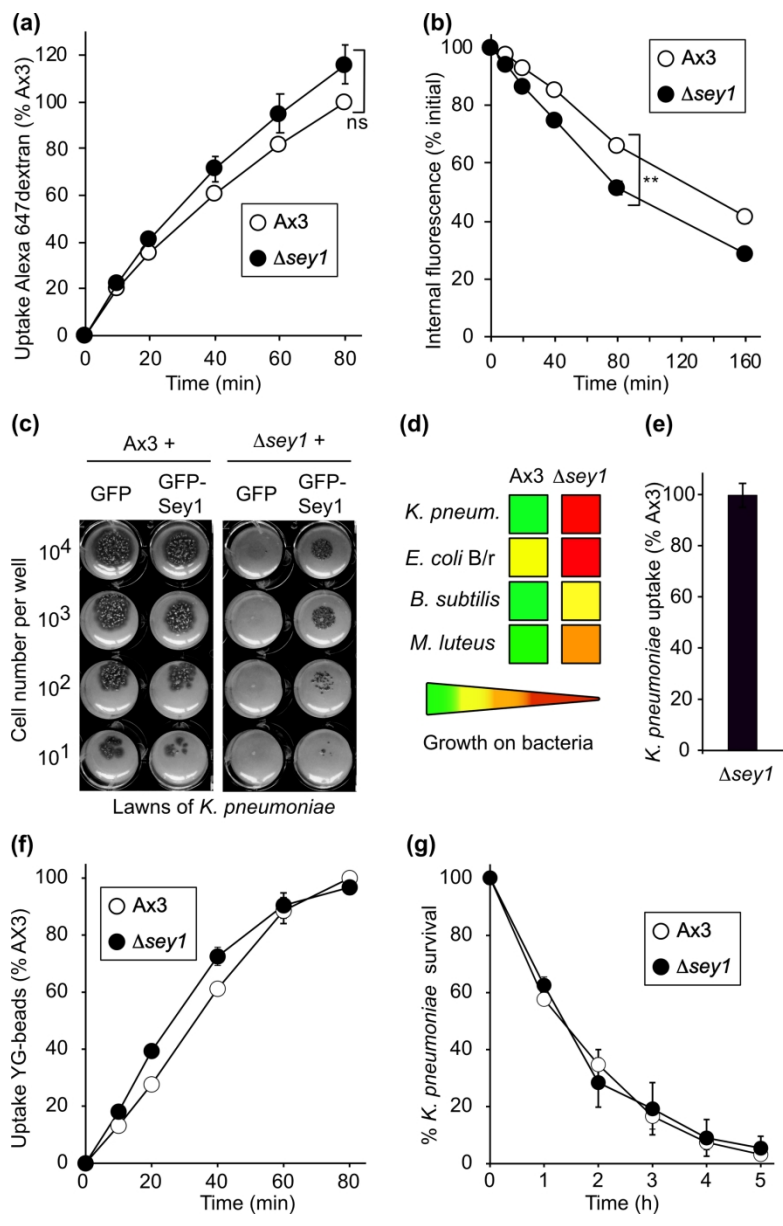


Figure 3

162x250mm (300 x 300 DPI)

1
2
3
4
5
6
7
8
9
10
11
12
13
14
15
16
17
18
19
20
21
22
23
24
25
26
27
28
29
30
31
32
33
34
35
36
37
38
39
40
41
42
43
44
45
46
47
48
49
50
51
52
53
54
55
56
57
58
59
60

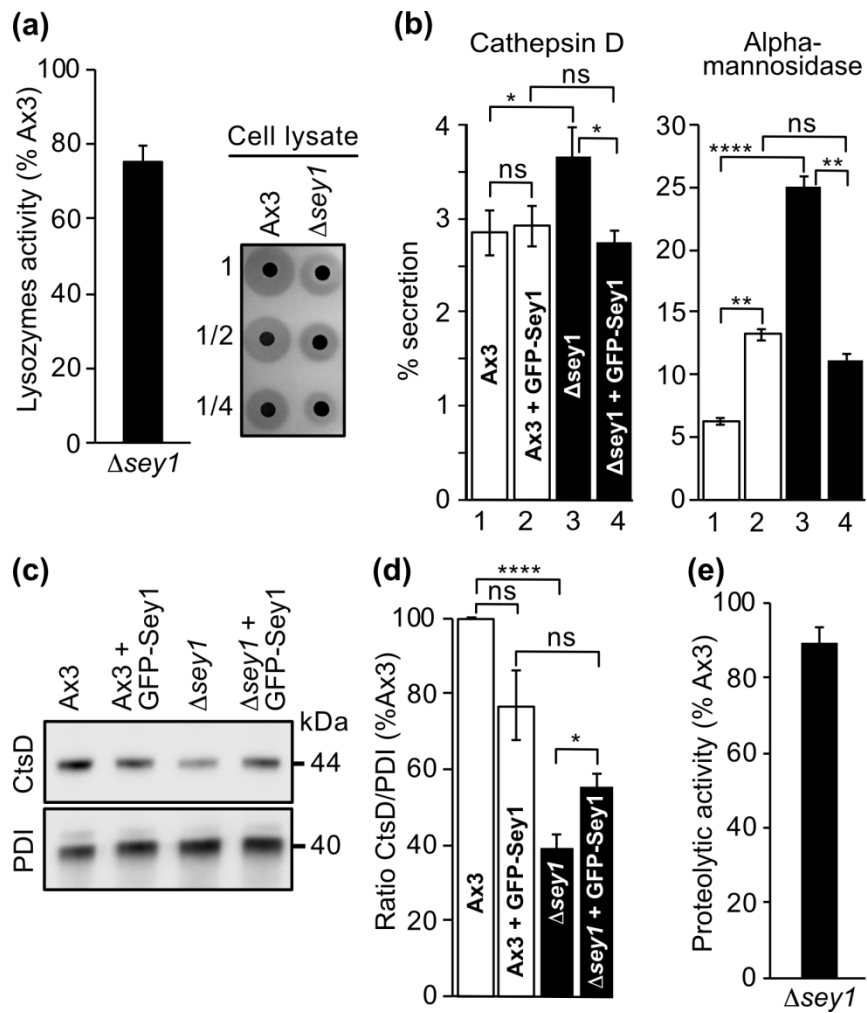


Figure 4

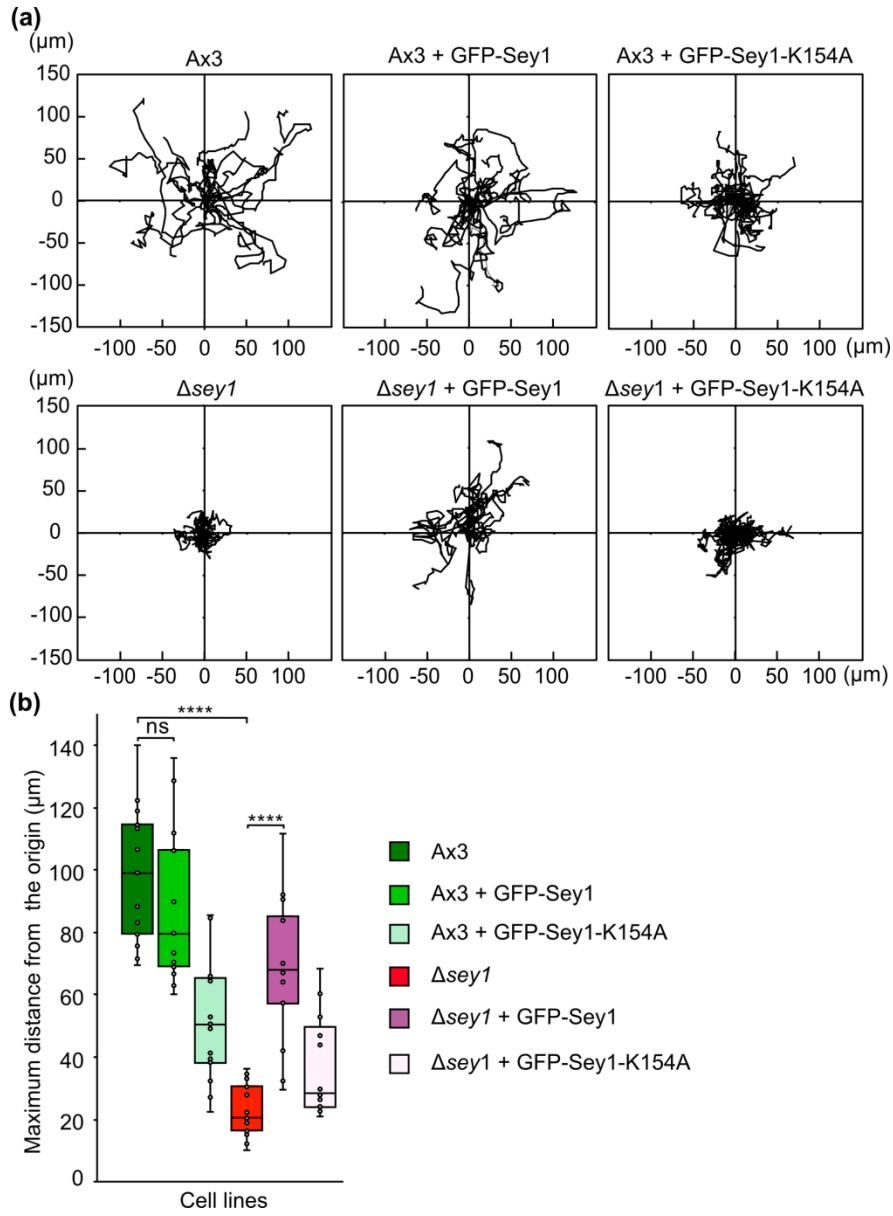


Figure 5

171x233mm (300 x 300 DPI)

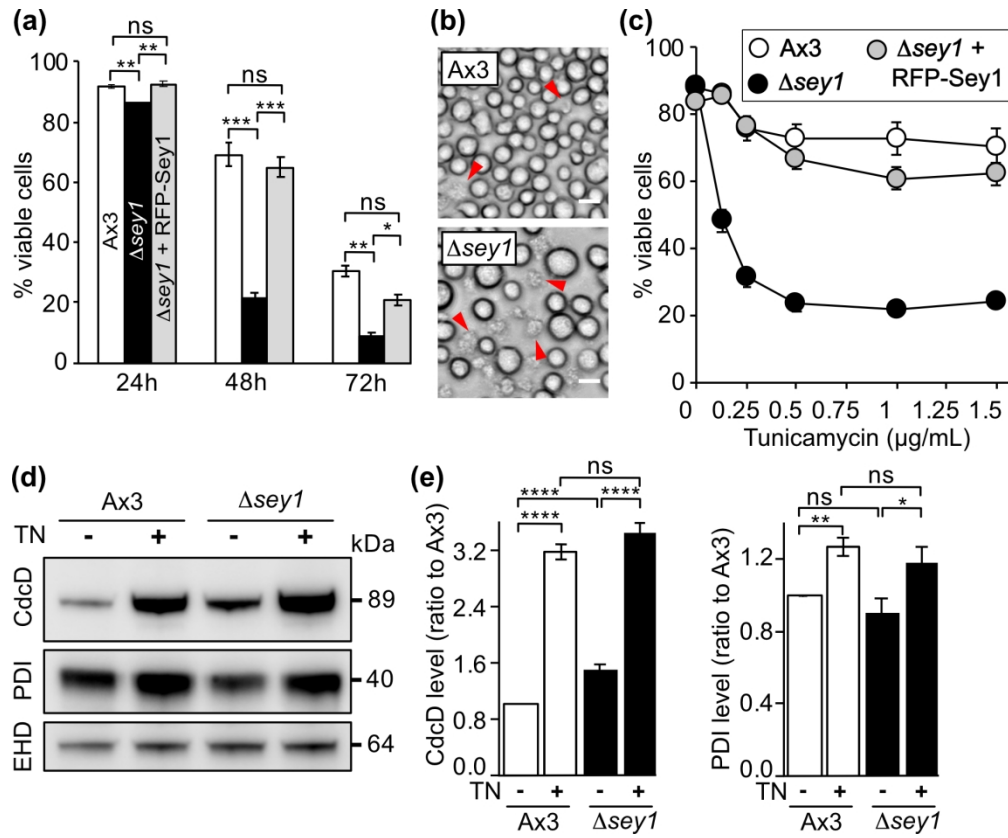


Figure 6

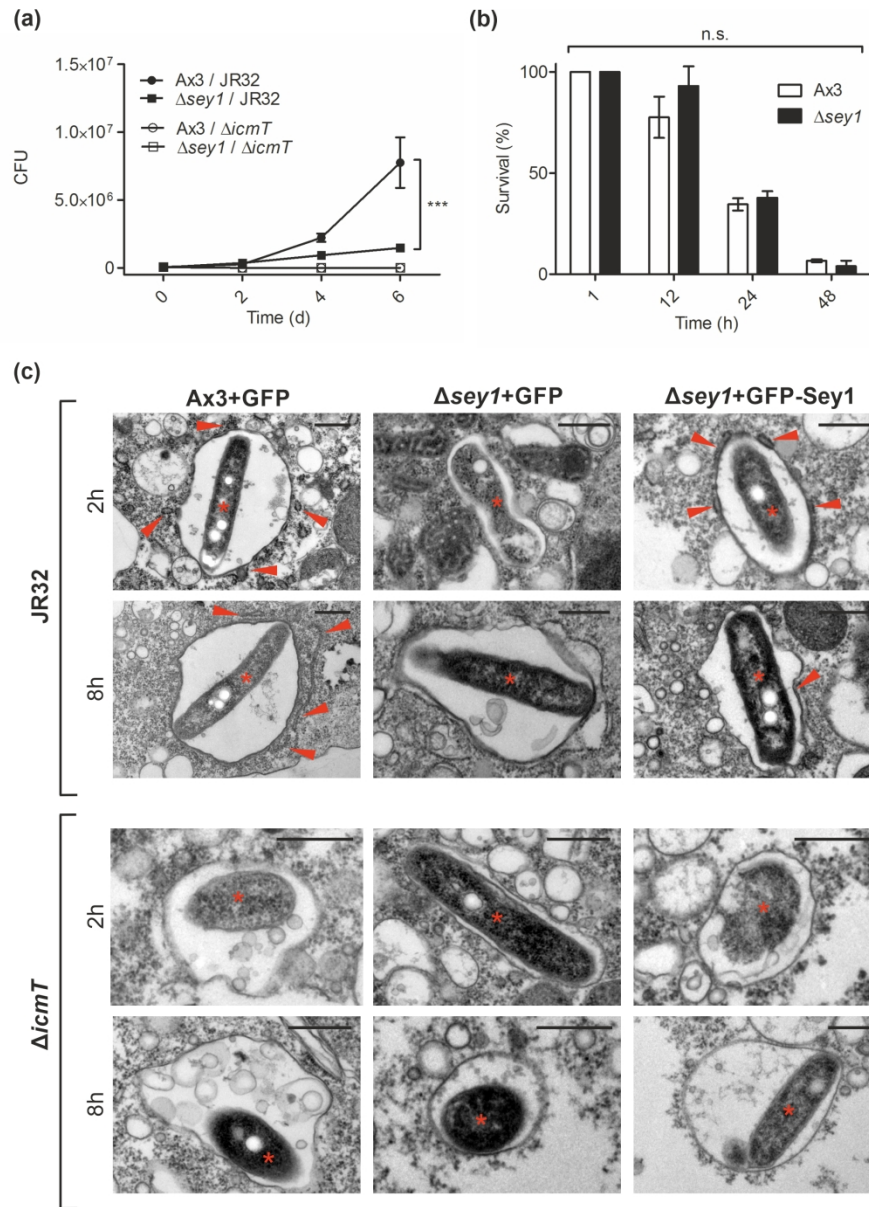


Figure 7

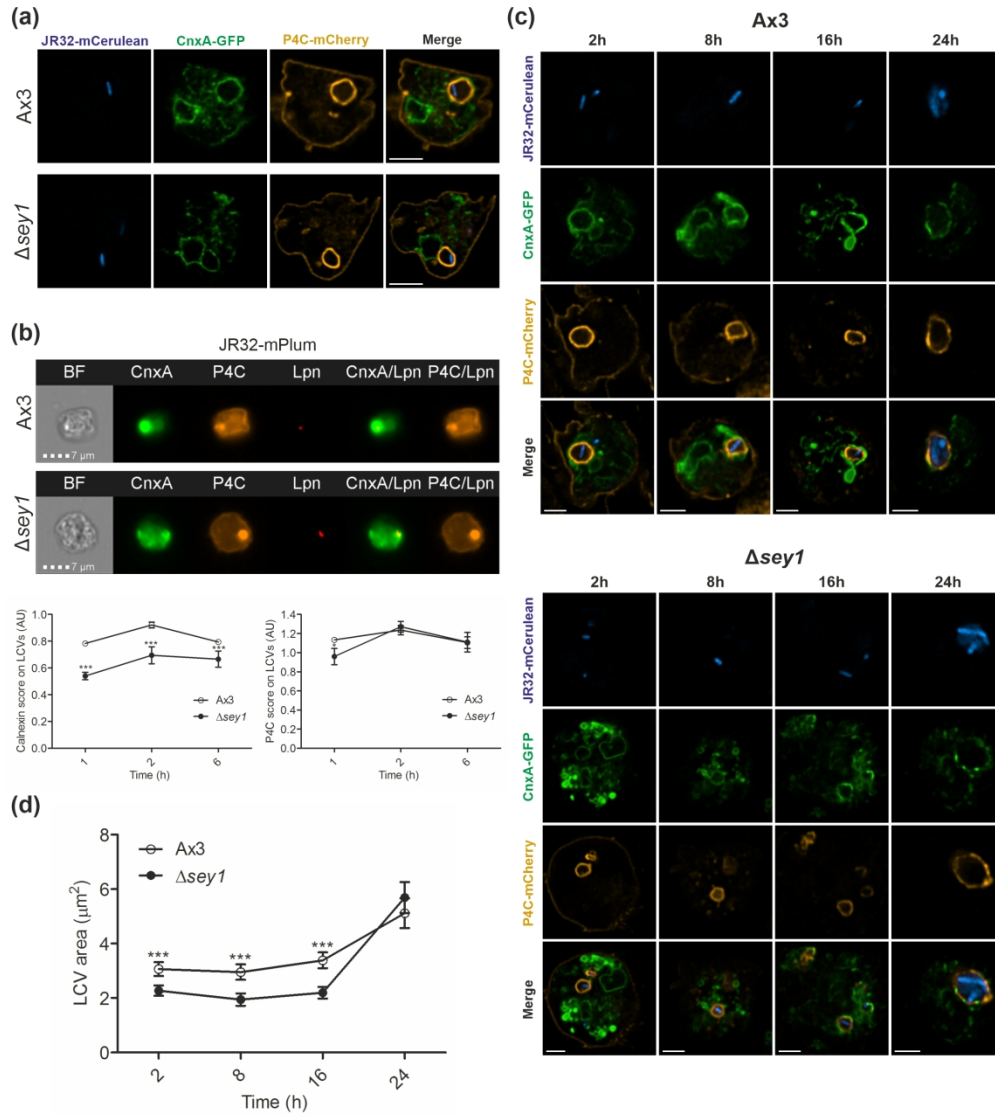


Figure 8